PLOS ONE

Design and validation of ultra-compact metamaterial-based biosensor for non-invasive cervical cancer diagnosis in terahertz regime

Musa N. Hamza[1]*, **Mohammad Tariqul Islam**[2]*, **Sunil Lavadiya**[3], **Iftikhar ud Din**[4], **Bruno Sanches**[5], **Slawomir Koziel**[6,7], **Md. Shabiul Islam**[8]*

1 Department of Physics, College of Science, University of Raparin, Sulaymaniyah, Iraq, 2 Department of Electrical, Electronic and Systems Engineering, Faculty of Engineering and Built Environment, Universiti Kebangsaan Malaysia, UKM Bangi, Selangor, Malaysia, 3 Department of Information and Communication Technology, Marwadi University, Rajkot, Gujarat, India, 4 Telecommunication Engineering Department, University of Engineering and Technology, Mardan, Pakistan, 5 Department of Electronic Systems Engineering, Escola Politécnica da Universidade de São Paulo, São Paulo, Brazil, 6 Engineering Optimization & Modeling Center, Reykjavik University, Reykjavik, Iceland, 7 Faculty of Electronics, Telecommunications and Informatics, Gdansk University of Technology, Gdansk, Poland, 8 Faculty of Engineering (FOE), Multimedia University (MMU), Cyberjaya, Selangor, Malaysia

* musa.nuraden@uor.edu.krd (MNH); tariqul@ukm.edu.my (MTI); shabiul.islam@mmu.edu.my (MSI)

Abstract

Cervical cancer belongs to the most dangerous types of cancers posing considerable threat to women's survival. It is most often diagnosed in the advanced stages as precancerous lesions are often symptom-free and difficult to identify. Microwave imaging, especially in terahertz (THz) range, is a convenient and noninvasive cancer detection tool. It enables characterization of biological tissues and discrimination between healthy and malignant ones. This study presents a novel triple-band biosensor based on metamaterials (MTMs). By leveraging unique properties of MTMs, the proposed biosensor operates as a perfect absorber. It exploits resonant modes in the THz spectrum to achieve remarkable sensitivity. Meticulous selection of the sensor geometry and dimensions enables efficient miniaturization. Meanwhile, utilization of frequency-domain data to detect refractive index changes improves resolution of cancerous tissue identification. Extensive numerical investigations corroborate its ability to carry out reliable early-stage cervical cancer diagnosis. This includes identification of the spatial extent of the malignant tissue. Excellent electrical properties of the sensor are accompanied by its compact size, which is highly desirable for non-invasive and portable applications.

1. Introduction

Cervical cancer is among the three primary malignant posing a significant threat to women's survival, with its fatality rate ranking third among cancer-related deaths in developing nations [1–3]. Persistent infection with carcinogenic strains of human papillomavirus (HPV) is the

leading cause of cervical cancer, resulting in the deaths of over 300,000 women annually, with nearly 90% of these fatalities in resource-limited countries. To address this disparity, there is a pressing need for targeted efforts in streamlined vaccination campaigns and the development of cost-effective, easily accessible screening methods. The World Health Organization advocates for the primary screening method to involve testing for high-risk HPV types, preferably using self-collected cervical-vaginal swab samples for efficient population screening. In situations with ample resources, an additional triage test is employed to refine the risk assessment for cervical precancer or cancer among HPV-positive individuals, constituting a screen-triage-treat strategy to mitigate overtreatment. Even in resource-limited settings, practical HPV screening is recommended, and a similar screen-triage-treat strategy is preferred over universal treatment, especially when balancing test sensitivity with minimal unnecessary interventions [4–6]. Cancer symptoms typically manifest when patients typically find themselves in the middle or advanced stages because precancerous lesions are often symptom-free and difficult to identify. Traditional testing approaches prove effective only when symptoms are evident, leading to increased patient suffering during treatment at these later stages. Various methods, including thinprep-cytologic-testing [7], uterine scraping [8], human papillomavirus screening [9] and vaginoscopy examination [10] can be employed for cervical cancer detection. To achieve a precise diagnosis report, a composite of these methods is commonly utilized, requiring the skills of an experienced medical professional. This indicates that the testing procedure is intricate, inconvenient, expensive, and time-intensive. Thus, the creation of a quick, uncomplicated, accurate, and efficient testing approach is highly important for the early-stage detection and diagnosis of cancers. The terahertz (THz) wave falls within the spectrum between microwaves and infrared region. Due to its low energy, it lacks ionization potential to harm living tissues or the human body. Additionally, as numerous biological macromolecules and polar molecules exhibit vibrational and rotational energy levels within the THz range, it serves as a valuable tool for characterizing biological tissues [11, 12]. Consequently, it has practical applications in medical diagnosis [13–16]. Typically, cancerous tissue exhibits a higher water content compared to normal tissue, and THz waves are readily absorbed by water. The absorption spectrum of THz waves can serve as a reliable method to differentiate between cancerous and normal tissues. Over the past two decades, there has been a growing interest surrounding THz time-domain spectroscopy (THz-TDS) technology. Numerous previous studies have highlighted the potential of THz technology in identifying various types of cancerous tissues, including colon cancer [17], liver cancer [18], blood cancer [19], breast cancer [20], and skin cancer [21–24]. This increased interest can be attributed to the consistent observation that cancerous tissues typically manifest higher absorption coefficients and refractive indices compared to their normal tissues [25–27]. Furthermore, THz imaging technology presents distinct advantages when contrasted with traditional detection methods. Notably, it possesses the ability to precisely sketch the boundaries of cancerous areas. This represents a notable advancement, as traditional techniques often fall short in providing such precise identification. Metamaterials (MTMs), are periodic sub-wavelength structures with a broad range of applications in imaging, antenna engineering and biosensing [28–30], and optoelectronics [31]. These materials have the capability to modify the fundamental principles of optics and electromagnetics [32, 33]. Specifically, metamaterial absorbers (MTMAs) are pivotal in the process of transforming incoming waves into thermal energy [34–36]. This characteristic allows for the detection and analysis of absorbed waves, making MTMAs essential in various applications [37, 38]. The investigation of metamaterials (MTMs) becomes imperative in addressing challenges arising from the lack of conventional electronic and quantum photonic responses in the terahertz (THz) frequency range. The development of a customized and controlled resonant response in metamaterials (MTMs) holds the potential to amplify interactions between

terahertz (THz) radiation and materials, leading to the emergence of novel capabilities and outstanding performance [39, 40]. The Metamaterials proposed in this article were utilized as perfect absorbers to design a biosensor with exceptional sensitivity to low refractive index variations. This innovative approach overtakes other absorber types, presenting the unique advantages of metamaterials in bio sensing applications. The proposed metamaterial perfect absorber enables precise detection of subtle changes in refractive index, making it an ideal surface for sensitive labeling. Unlike traditional absorbers, this metamaterial-based biosensor offers enhanced performance, creating the way for more efficient and accurate detection methods in various fields, particularly in bioscience and medical diagnostics where slight variations play a crucial role in accurate analyses. Over the years, metamaterials have found application in the development of various sensors across different fields: Yang et al. presented a THz sensor with tunable characteristics, employing two concentric split-ring resonators. The sensor demonstrated a tuning range spanning from 0.958 to 1.390 THz [41]. Saadeldin et al. introduced a novel MTM (metamaterial) absorber design for THz (terahertz) applications related to sensing in the biomedical field. The sensor demonstrated an impressive 99% absorptivity specifically at 2.249 THz, accompanied by a Q-factor of 22.05. Additionally, it exhibited a sensitivity of 23.7 GHz/µm when employed for measuring analyte thickness [42]. Wang investigated a prototype designed for sensing applications, consisting of two identical square patches made up of unit cells. The suggested configuration achieved close to 100% absorption at frequencies of 1.7780 and 2.4591 THz, accompanied by quality factors of 6.9156 and 296.2771, respectively [43]. Azab et al. offered a thorough examination of optical biosensors designed specifically for the early detection of cancer, incorporating metamaterial sensors within their comprehensive overview [44]. Geng et al. introduced a micro-ring metamaterial resonator that incorporates microfluidics for the detection of biomarkers related to liver cancer. The resonator exhibited a significant maximum frequency shift of 14 GHz when exposed to a concentration of 0.025 µg/ml [45]. In this letter Banerjee et al. introduced a biosensor using two circular ring resonators, demonstrating a high sensitivity of 1500 GHz/RIU and a FOM of 25 RIU-1. This emphasizes its effectiveness in cancerous cell detection with a favorable trade-off between sensitivity and overall performance [46]. Vafapour et al. [47] presented a bio sensor designed for colon cancer detection using a water-based system. Moreover, another sensor utilizing a graphene-based metamaterial demonstrated sensitivity towards various cancer cell types, achieving a sensitivity of 207 GHz/RIU, a FOM of 3.86 RIU-1 and Q of 13 [48]. Moreover, Askari et al. [49] presented an extremely responsive sensor utilizing metamaterial, characterized by its sensitivity of 4077.2 nm/RIU operating in the frequency range between 150 and 500 THz. In [50] Bhati et al. introduced a specialized metamaterial sensor designed for the identification of cancerous cells, displaying a sensitivity of 1462 GHz/RIU. Ma et al. [51] also contributed significantly with their proposal of a refractive index metamaterial sensor characterized by high sensitivity, measuring at 2372 GHz/RIU. However, triple-band sensors both, offering broader coverage, heightened versatility, superior performance, and increased sensitivity in detecting the THz spectrum. This makes triple-band sensors more advanced and effective across various applications compared to their single and dual-band. Recent studies have demonstrated ultra-thin hepta-band metamaterial absorbers with high absorption efficiency across multiple THz frequencies, highlighting the potential of such designs for sensing applications [52]. Additionally, the development of ultra-compact polarization-sensitive triple-band microwave absorbers supports the multi-band absorption characteristics of our proposed biosensor [53]. Graphene-based tunable metamaterial absorbers have shown high absorption efficiency and tunability in the THz range, which aligns with our sensor's ability to discriminate between healthy and malignant tissues based on dielectric properties [54]. Furthermore, research on ultra-thin metamaterial perfect absorbers for single, dual, and multi-

band applications reinforces the versatility and effectiveness of these designs, paralleling our sensor's performance in the THz spectrum [55]. Lastly, studies on quad-band polarization-sensitive THz metamaterial absorbers provide insights into achieving high sensitivity and accuracy, which are crucial for our non-invasive cervical cancer diagnosis sensor [56].

In this manuscript presented an advanced diagnostic tool, the design of an exceptionally compact Triple-band Biosensor based on Metamaterials (MTMs) operating in the Terahertz (THz) region represents a novel innovation for Cervical Cancer diagnostics. Utilizing the unique properties of MTMs, this biosensor serves as a perfect absorber, exploiting resonant modes in the THz spectrum to achieve exceptional sensitivity. The discussion extensively explored various models, investigating factors such as polarization and the distribution of electric and magnetic fields. Of particular significance was the application of terahertz waves as a compelling approach for early cancer imaging. This promising method holds the potential to revolutionize non-invasive diagnostics, helping in transformative advancements in early cancer detection and subsequent treatment strategies. The triple-band configuration ensures precise and simultaneous detection of specific disease sign associated with cervical cancer, enhancing the diagnostic accuracy. The miniature size of the biosensor, facilitating non-invasive and portable applications, makes it an ideal candidate for point-of-care diagnostics, holding great potential for early detection.

2. Model's unit cell layout

The input signal of the THz structure carries information and energy. The incident wave interacts with the structure, which causes absorption, transmission, and reflection. The metamaterial-inspired structure helps for the absorption of EM waves. The minimum reflection indicates a maximum absorption of inputs. The transmitted waves pass through the structure absorb maximum energy and reduce transmission. The absorption using the proposed design helps to control transmission characteristics. The response of sensitivity, specificity and selectivity were taken into consideration during the design of the biosensor. The effectiveness of the sensor depends upon these variables. The challenging aspect for the sensor is to enhance specificity and sensitivity. To enhance clinical data and meaningful value for cancer detection optimisation of structure is required.

The proposed optimised design structure is represented in Fig 1(C). The optimized structure was designed based on structures shown in Fig 1(A) and 1(B). Fig 1(A) shows a model 5 structure. Fig 1(B) shows the Model 2 structure. The Aluminum (Al) metal material is chosen
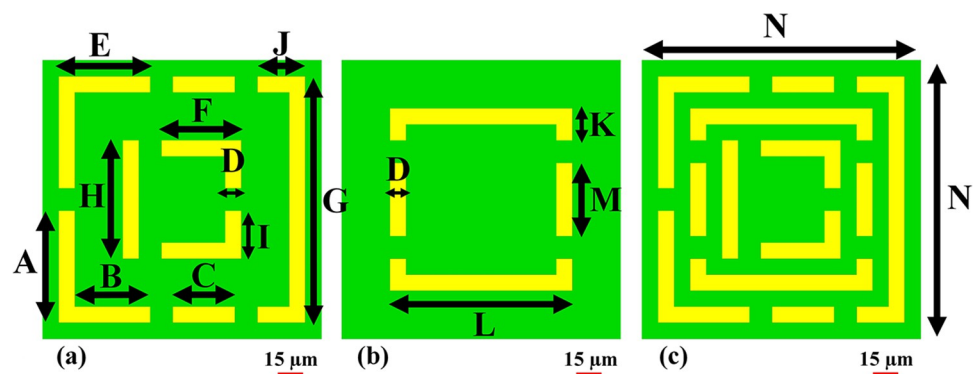
Fig 1. Recommended structural design for a perfect absorber; (a) model 5, (b) model 2, and (c) model 10 (proposed biosensor design).

https://doi.org/10.1371/journal.pone.0311431.g001

Table 1. A complete list of the variables that have been adjusted for the recommended sensor.

Parameter	Value (μm)	Parameter	Value (μm)
A	74.2	J	32
B	50	K	21.2
C	41.1	L	121
D	10.6	M	48.5
E	60.5	N	185
F	53	Polyimide thick (T_1)	125
G	163.3	Coverslip thick (T_2)	4
H	78.5	HeLa Cells thick (T_3)	14
I	32	Aluminum (Al) thick	0.2

https://doi.org/10.1371/journal.pone.0311431.t001

as the conducting material and polyimide material is chosen as the substrate material. In the proposed structure the Aluminum metal is employed as the top and bottom layers of the model's three-layered construction, with a polyimide dielectric spacer serving as the intermediate layer. The Aluminum has a conductivity of 3.56×10^7 S/m, and the dielectric spacer was 125 μm thick. The Al layers were 0.2 μm thick on top and bottom.

The combination of two structures helps reduce interfacing and overlapping of magnetic and electric forces. The dimensions of different parameters are represented in Table 1. The suggested absorber was constructed using a commercial full-wave finite integration approach (FIT) based on EM solver computer simulation technology (CST) in the microwave studio. Metamaterials (MTMs) may be analyzed using numerical computations to identify their properties and how they function across various frequency ranges and boundaries. Scientists have used numerical analysis to analyze various structures such as free space, unit cells, perfect electric and magnetic conductors, as well periodic arrays. To simplify simulation methods, a unit cell was allocated in the x and y-axis, with an open add-space in the z-axis.

To maximize power penetration and propagation in polyethene terephthalate (PET), the top metal layer was designed to match its impedance with the incident medium. To understand the transmission-line theory (TLT), the bottom AI layer is designed to block all incident electromagnetic (EM) waves and give zero impedance. The metallic layer at the bottom prevents transmission, and absorption devices with large electrical and/or magnetic losses collect moving waves. A top-plane electromagnetic (EM) wave was used to attain the absorption values.

3. Results and discussion

This section aims in the comparative analysis of a wide range of compact absorber-based sensors targeting the operation in the Sub THz regime. To adequately cover the rich amount of possible architectures, in this work, ten different component designs are incrementally presented, simulated and evaluated with respect to its absorption spectrum, power flow and field density. The first design addressed is derived from a modified square shaped split ring resonator. One possible implementation is shown in Fig 2(A), where it was also simulated and its absorption curve was plotted in respect to the frequency. The absorption characteristics of the model presented two resonances, one at 0.7 THz and other near 0.95 THz, but the absorption peaks were far from ideal and a new set of absorber strategies were developed. A modified design was developed using a reduced symmetric split ring, targeting to achieve stronger absorption. This design was labeled Model 2 and is presented in Fig 2(B) together with its simulated absorption curve. Model 2 absorption curve also presented 2 peaks, but in this version,
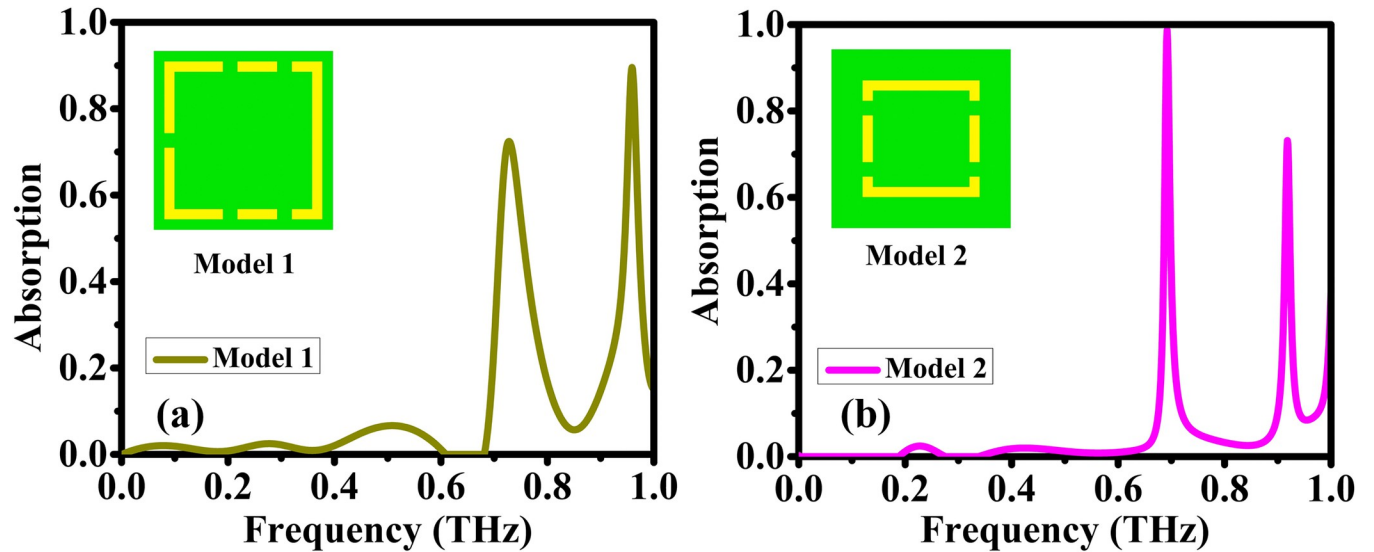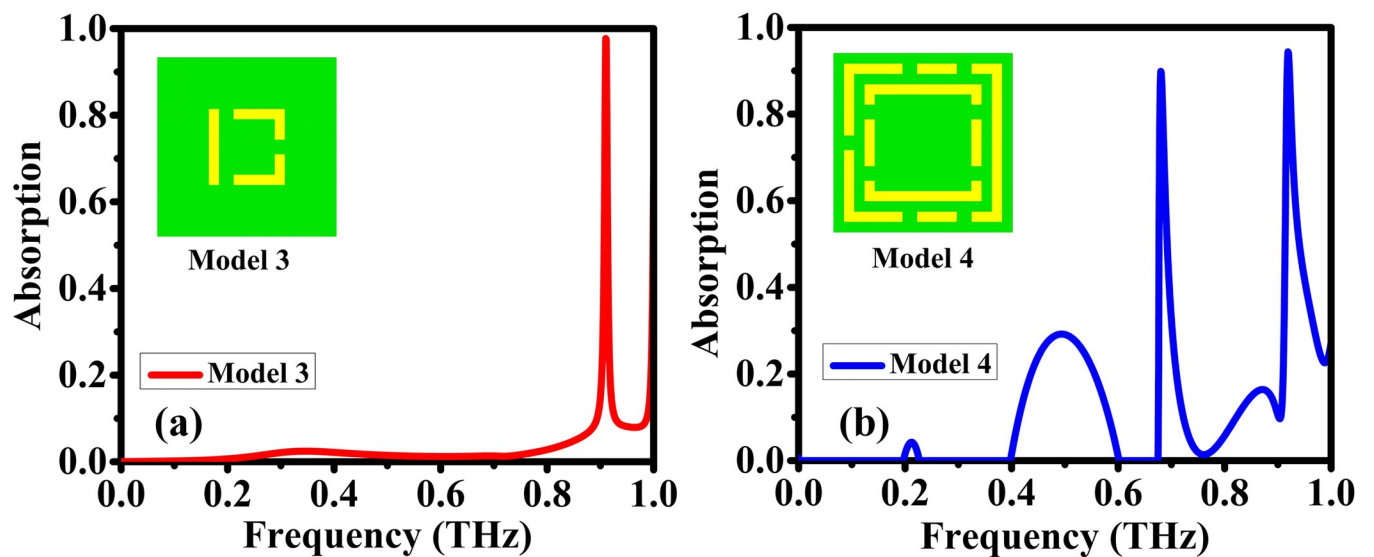
Fig 2. Comparison between the absorption properties of the two initial split ring designs: (a) shows the Model 1; and (b) shows the reduced symmetric ring version labeled as Model 2.

they were very narrower and the simulation resulted in much improved characteristics in the absorption peak at 0.7 THz.

Targeting to obtain a better absorber at near THz frequency, two additional alternatives were designed. Model 3 consists of a D shaped split ring dipole and Model 4 is based on a dual ring approach mixing the characteristics of the previously studied Models. Fig 3 presents the design layout and the absorption curves for Model 3 and Model 4. The results for Model 3 presented an almost ideal absorption around 0.92 THz, being this design a very important candidate to compose the final sensor. Model 4 showed dual absorption peak characteristics in well behavior frequency locations, but with not near perfect absorbance. The promising results of Model 3 and the mixed output peaks found in Model 4 using its bi-component design

Fig 3. Comparison between the absorption properties of the Model 3 and Model 4 designs.
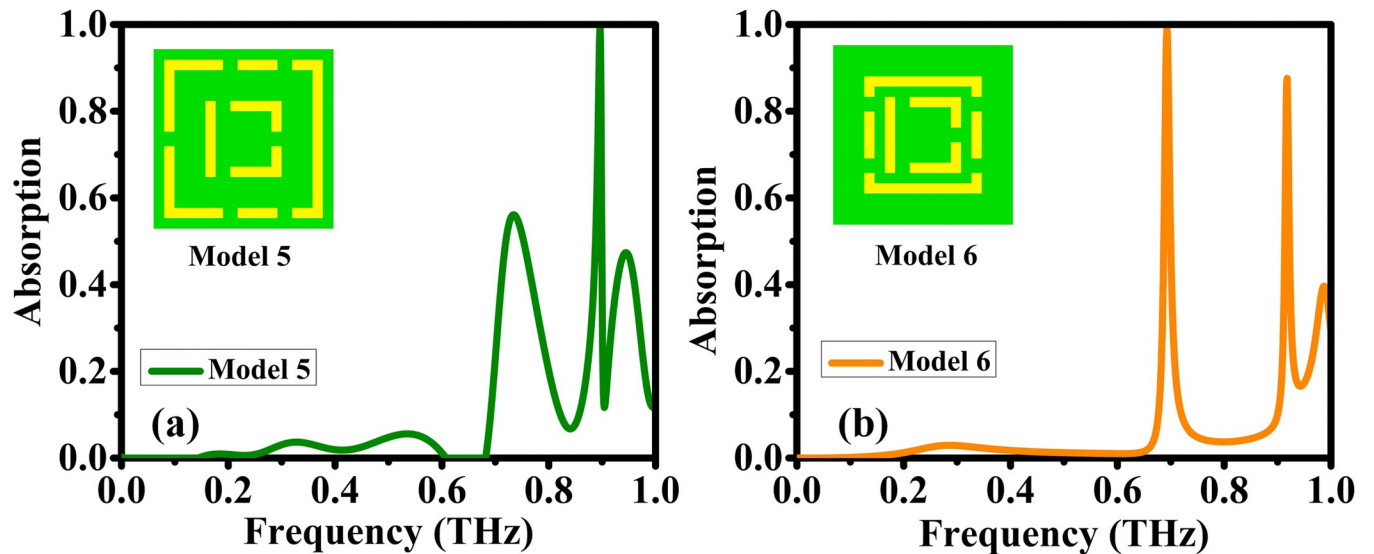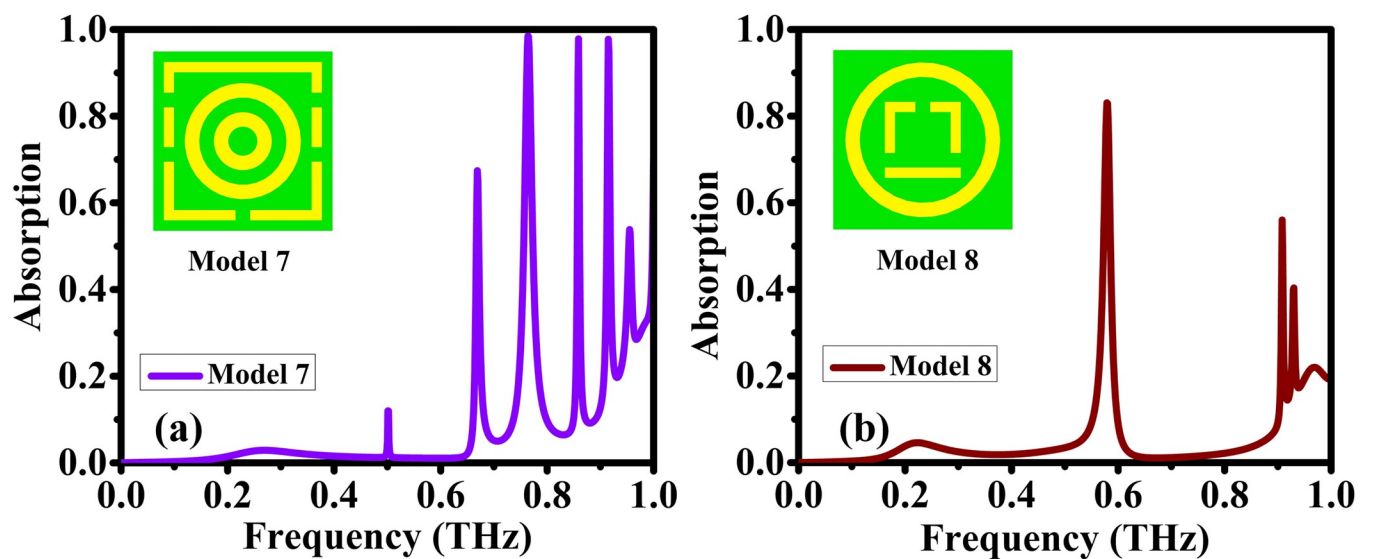
Fig 4. Absorption characteristics of mixed models: (a) Model 5; and (b) Model 6.

triggered the design of two more versions of the absorber, basing them in the combination of the constituents of the Model 1 and Model 3 generating the Model 5 and with Model 2 and Model 3 generating the basis for Model 6. The combined designs Model 5 and Model 6 and its absorbance curves are presented in Fig 4.

The absorption curve obtained from Model 5 presented slightly better results in 0.88 THz in comparison to Model 3, but now it also has wide untuned side absorption sections. The results for Model 6 also presented the dual peaks seen before in Models 1 and two, but with improved absorbance.

In order to provide a good coverage of the design options, mixed structures with circular rings were also investigated. Model 7 proposes an alternative using double circular rings in together with a split ring external section, as shown in Fig 5(A). On the other hand, Model 8

Fig 5. Absorption characteristics for the designs with circular shaped structures: (a) Model 7 and (b) Model 8.

tests the opposite case where the D shaped ring was maintained and used along with an external circular ring, as explain in Fig 5(B).

Model 7 with its triple element approach generated strong absorption in three main frequencies around 0.75 THz, 0.85 and 0.91 THz. Unfortunately, the results from the Model 8 were not adequate, and this directed the efforts to keep with the external rectangular split ring design. Two final design options were developed trying to achieve near three band THz absorption uniting the qualities of the triple element design, but without the fabrication difficulties of the circular structure and using the previously explored external split ring. Fig 6(A) presents an alternative design for the absorber labeled as Model 9 which uses losanges in place of the circular rings. Finally, Fig 6(B) shows Model 10, which comprises the integration of the D shaped internal structure (initially tested in Model 3) with the dual external rectangular split ring resonators. Fig 6(A) shows the simulation results of Model 9 which presented multiple absorption peaks, but just the band near 0.71 THz was near ideal. On the other hand, the absorption curve of Model 10 presented near perfect absorption characteristics in a triple band fashion including peaks at 0.684 THz, 0.918 THz and 0.971 THz. The structural design of Model 10, in conjunction with its mixed approach reusing several previously optimized subdesigns was very successful in the near THz range and was selected as a proposed model to be evaluated as the main biosensor of this work.

To complete the analysis of the proposed resonator-based sensor, a set of simulations were made targeting to cover some possible available materials for fabrication of the device, both the substrate material and the conductor metalization options were tested and the results are presented in Fig 7.

The simulated substrate materials were FR4, Polyimide, Arlon AD 410/430 and the famous Rogers Duroid RT 5870. Fig 7(A) shows very mixed results for this case, favoring Arlon and Polyimide. Deeper optimizations could be made for each specific case, but in order to direct the resonator to the biological application, an easily available polymer with good coupling was selected, the Polyimide.
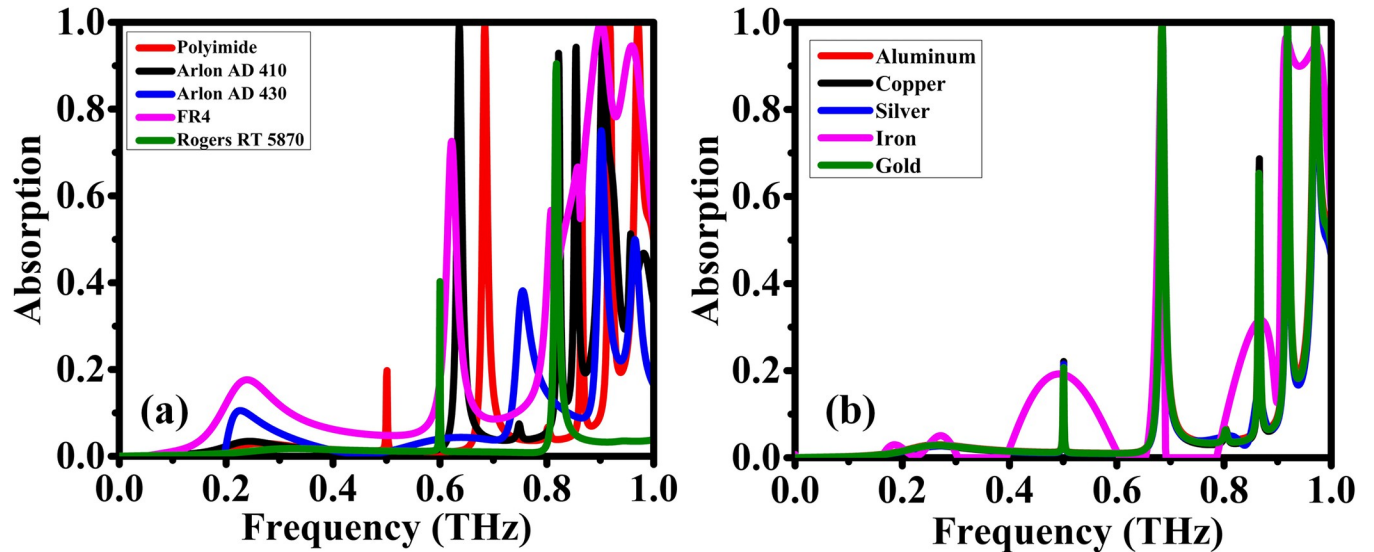
In relation to choice between the different available metals, most of the tested materials would be acceptable to be used, except for Iron. The simplicity of production and low cost of
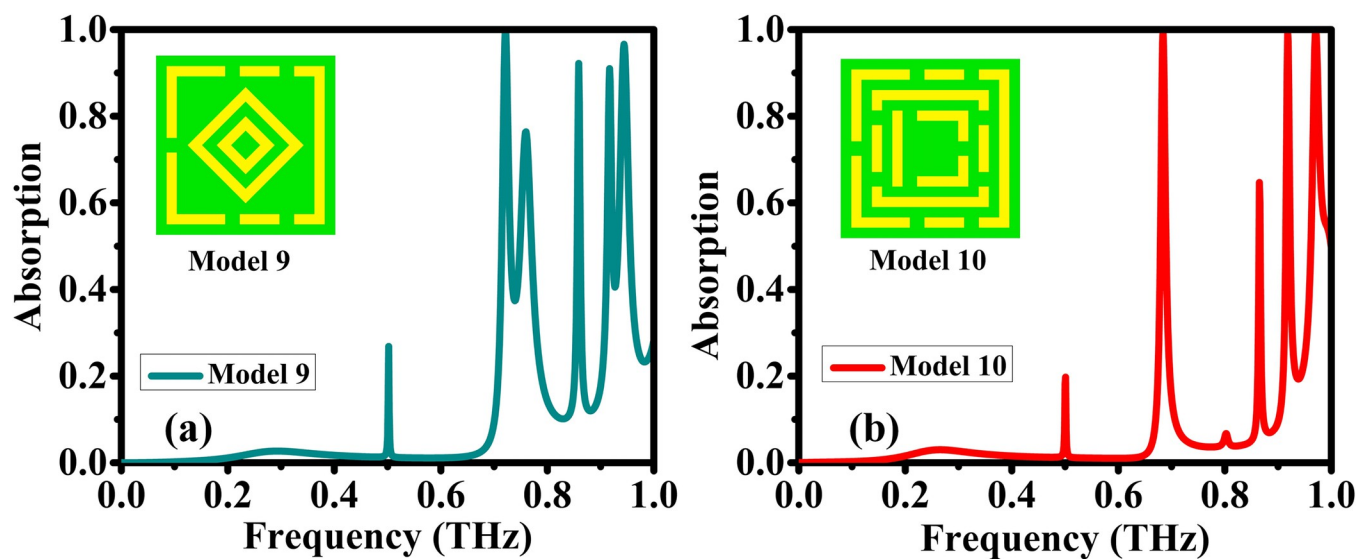
Fig 6. These are the two designs' distinct absorption characteristics: (a) Model 9; and (b) Model 10 (purpose biosensor).

https://doi.org/10.1371/journal.pone.0311431.g006

Fig 7. Absorption spectra for the proposed design under various: (a) substrate material and (b) resonator material conditions.

https://doi.org/10.1371/journal.pone.0311431.g007

material, together with the good simulation results guided the current choice to Aluminum, as explain in Fig 7(B).

This investigation delves into the performance nuances of a metamaterial biosensor concerning varying incident and polarization angles, specifically tailored for terahertz imaging in early cancer detection. Despite minor fluctuations, a robust, angle-independent feature consistently manifests across both incident and polarization analyses (Fig 8(A) and 8(B)), showcasing remarkable angular insensitivity. This intrinsic characteristic ensures uniform biosensor responses irrespective of incident wave angles or polarizations, underscoring its resilience and applicability in real-world scenarios. Despite slight variations in incident angles, a consistent and angle-independent feature, denoted by a dense red line in Fig 8(A), underscores the biosensor's sensitivity to diverse angles of incidence. Polarization angle analysis (Fig 8(B)) reveals minimal deviations from incident angle results. The incident angle, representing the impact angle of the incident electromagnetic wave on the biosensor surface, holds significance in
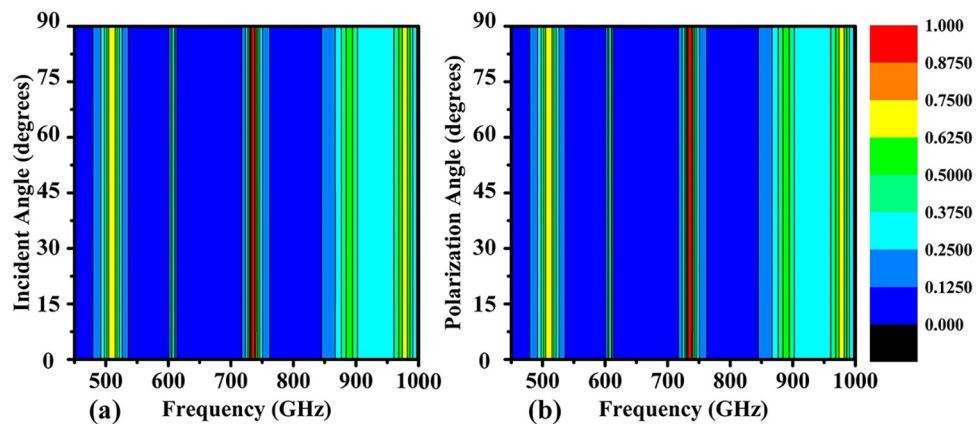
Fig 8. The impact of angle modification on absorption rate is investigated for: (a) incidence angle and (b) polarization angle.

https://doi.org/10.1371/journal.pone.0311431.g008
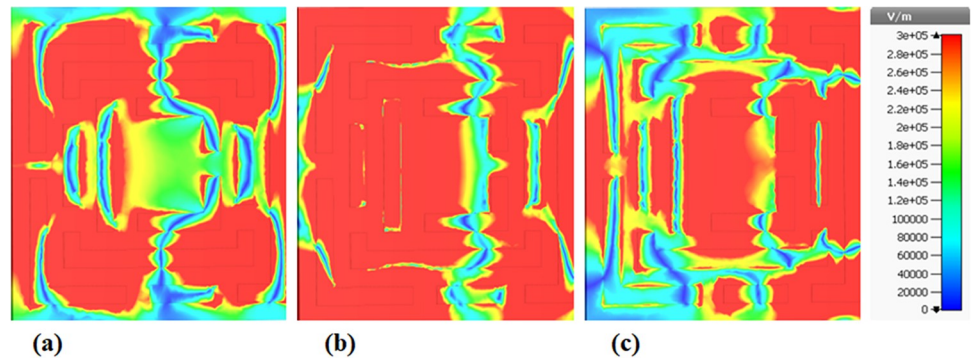
Fig 9. Distributions of the metamaterial structure field are shown on a colour map: (a) E-field at 0.684 THz, (b) E-field at 0.918 THz, and (c) E-field at 0.971 THz.

influencing interaction dynamics and signal specificity in terahertz imaging. Simultaneously, the polarization angle, indicating the orientation of the incident wave's electric field vector, plays a crucial role in shaping the biosensor's response to terahertz waves. The interplay between incident/polarization angles and the signal-to-noise ratio (SNR) emerges as crucial, where optimal angles and polarizations maximize signal strength and minimize noise, leading to heightened SNR. The observed angle-insensitivity, coupled with meticulous SNR optimization, attests to the exceptional efficacy of this metamaterial biosensor for robust terahertz imaging in early cancer detection.

In Fig 9, the presented images illustrate a significant electric field intensity ranging from 20,000 V/m to 300,000 V/m within a metamaterial biosensor, with notable resonances at 0.68 THz, 0.918 THz, and 0.971 THz. The spatial distribution of the electric field likely corresponds to or proximate to these resonance frequencies, unveiling distinct high (red) and low (blue) intensity regions. These variations suggest localized interactions between terahertz waves and the metamaterial, featuring intricate patterns indicative of intentional design for optimized biosensing. Each spectrum peak correlates with a resonance, demonstrating efficient coupling between the metamaterial and terahertz waves, concentrating the electric field. Strategically positioned high-intensity regions hold potential for interactions with cancer-specific biomolecules crucial for early detection. The triple resonance peaks indicate multi-band functionality, enabling detection of various cancer-related biomolecules at distinct frequencies within the 0.68–0.97 THz range. Analyzing electric field distributions for each resonance provides insights into field localization and resonant behavior across bands, offering opportunities for targeted biomarker detection. Fig 9(A)–9(C) likely depict electric field distributions within the biosensor at resonant frequencies (0.68 THz, 0.918 THz, and 0.971 THz) designed for early cancer detection. Spatial distributions reveal high-intensity (red) regions concentrated due to resonance and low-intensity (blue) regions, with complex patterns signifying interactions with surrounding tissues and potential biomarkers. Resonant behavior at each frequency corresponds to optimal coupling, resulting in enhanced electric field, particularly in high-intensity regions. Analyzing the location and intensity distribution across figures provides crucial insights into the biosensor's detection capabilities at different frequencies, crucial for early cancer diagnosis.

Observed magnetic field intensity variations between 100 A/m and 1000 A/m in Fig 10(A)–10(C) suggest significant enhancements within the metamaterial structure at resonances around 0.68 THz, 0.918 THz, and 0.971 THz. The spatial distribution of the magnetic field at these frequencies shows both high and low intensity regions, suggesting localized interactions
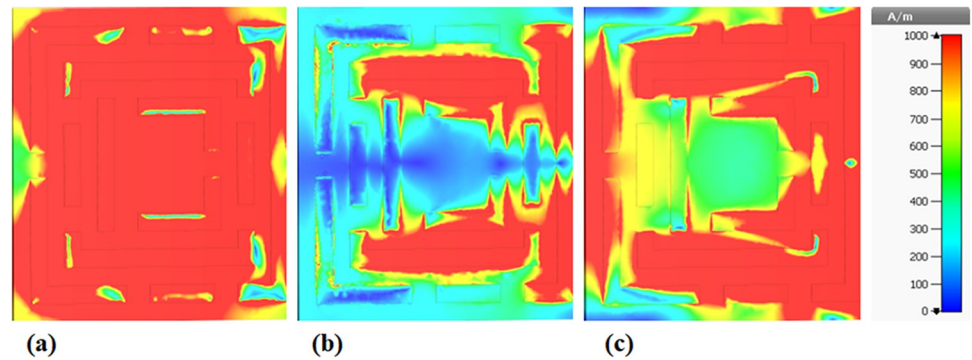
Fig 10. An illustrated colour map shows the field distributions of the proposed metamaterial structure: (a) H-field at 0.684 THz, (b) H-field at 0.918 THz, and (c) H-field at 0.971 THz.

between terahertz waves and the metamaterial. These patterns indicate intentional design features for optimized biosensing. High-intensity regions may facilitate interactions with cancer-specific biomolecules for early detection. The complex patterns in the H-field distribution are likely influenced by the metamaterial's design, including materials, structure, and dimensions. Understanding these design aspects is crucial for interpreting field localization and overall biosensing performance. The triple-band functionality of the biosensor suggests potential detection of various cancer-related biomolecules at different frequencies within the 0.68–0.97 THz range. Analyzing H-field distributions for all three peaks could reveal differences in field localization and resonant behavior across bands, providing insights into targeting specific biomarkers.

The electric and magnetic field distributions within our metamaterial-based biosensor are pivotal for detecting cancer-specific biomolecules in the terahertz regime. Leveraging a triple-band design, the biosensor generates localized regions of heightened electric fields within its cavity, facilitating enhanced interactions with polar biomolecules prevalent in cancer cells, such as proteins and nucleic acids. This intensified interaction results in elevated terahertz absorption by cancerous tissues compared to healthy counterparts. Additionally, magnetic field analysis provides essential spatial sensitivity, enabling precise localization and assessment of cancerous lesions. While establishing definitive electric field intensity thresholds for clinical applications presents challenges due to biological variability, ongoing research aims to further elucidate these relationships through comprehensive studies with biological samples, aiming to enhance diagnostic accuracy and clinical efficacy.

To gain a deeper understanding of the physical absorption mechanisms inherent in the proposed metamaterial absorbers, an examination of the surface current distribution within the upper layers of the recommended design was undertaken. The presence of circular antiparallel current flow was identified, indicative of a robust magnetic response. Fig 11(A) elucidates a magnetic dipole resonance mode, portraying parallel and antiparallel surface current patterns at 0.68 THz. Furthermore, Fig 11(B) and 11(C) delineate the current distributions corresponding to the second resonance modes at 0.918 THz and the third resonance modes at 0.971 THz, respectively, both exhibiting pronounced magnetic responses. The interplay between parallel and antiparallel current flows within these distributions governs the resultant electric and magnetic field distributions, contributing to the opposition between internally generated and externally incident magnetic fields (H-field). A comprehensive examination of power flow was conducted at the surface area of the recommended sensor. Meanwhile, observed variations in surface current intensity ranging from 10 A/m to 100 A/m in Fig 11(A)–11(C) signify
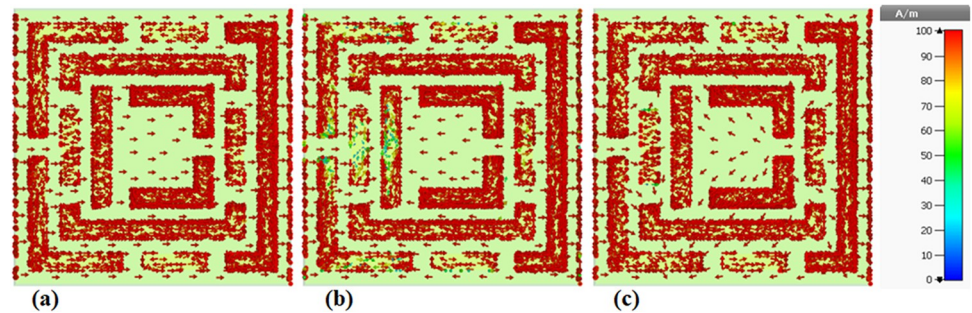
Fig 11. The surface current distribution of the recommended metamaterial design: (a) at 0.684 THz, (b) at 0.918 THz, and (c) at 0.971 THz.

https://doi.org/10.1371/journal.pone.0311431.g011

substantial enhancements within the metamaterial structure, particularly at resonances around 0.68 THz, 0.918 THz, and 0.971 THz. These figures are interpreted as spatial representations of surface current distributions, revealing regions of both high (red) and low (blue) intensity, indicative of localized interactions with terahertz waves. The intricate patterns observed are a result of intentional design features aimed at optimizing biosensing performance. Each resonance peak within the spectrum corresponds to efficient coupling, strategically concentrating surface current density for potential interactions with cancer-specific biomolecules.

The triple-band metamaterial biosensor exhibits a compelling power flow profile, particularly at resonances of 0.68 THz, 0.918 THz, and 0.971 THz, emphasizing its efficacy in early cancer detection. The power flow analysis, depicted in Fig 12(A)–12(C) for each resonance point, underscores the biosensor's robust capability. These results affirm intense power flows, especially at the resonant frequencies, indicative of the biosensor's proficiency in detecting cancer cells. The intentional design of the biosensor strategically amplifies power flow, ranging from 10,000,000 V.A/m^2 to 100,000,000 V.A/m^2, as observed in the metamaterial absorbers. The intricate patterns in the power flow distribution highlight deliberate design features for biosensing applications. The high-power flow of the biosensor holds crucial advantages for terahertz imaging. By concentrating power flow at specific resonances, the biosensor enhances sensitivity, allowing for targeted interactions with biomolecules. This focused power flow within the metamaterial structure aligns with the shared principle of resonant enhancement in terahertz imaging, amplifying the potential for biomolecule detection. The triple-band functionality further broadens the biosensor's utility, promising the detection of cancer-related biomolecules across the 0.68–0.97 THz range. The correlation with terahertz imaging
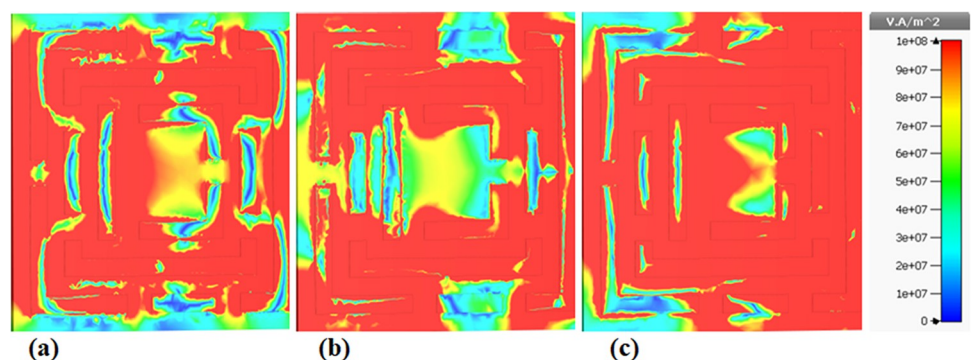
Fig 12. An examination of the power flow at: (a) at 0.684 THz, (b) at 0.918 THz, and (c) at 0.971 THz.

https://doi.org/10.1371/journal.pone.0311431.g012
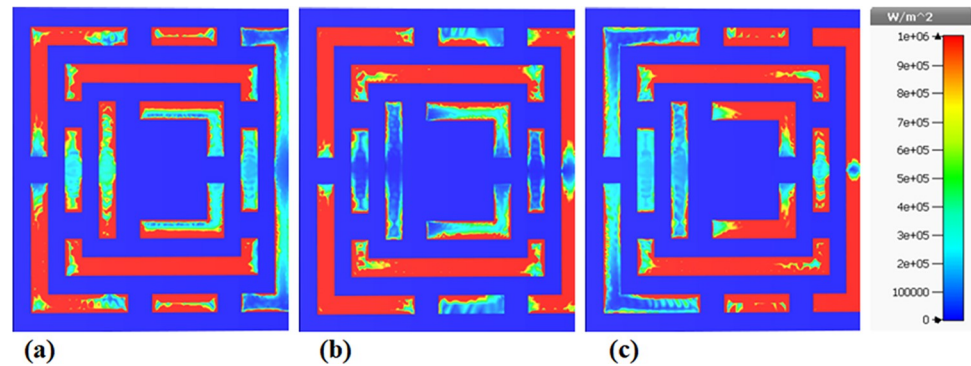
Fig 13. An examination of the surface power loss at: (a) at 0.684 THz, (b) at 0.918 THz, and (c) at 0.971 THz.

https://doi.org/10.1371/journal.pone.0311431.g013

underscores the biosensor's emphasis on metamaterial power flow enhancements, showcasing its unique approach centered on directing and intensifying power flow for optimal interactions with terahertz waves and subsequent indirect cancer biomolecule detection.

The elucidation of surface power loss patterns in Fig 13(A)–13(C) at resonant frequencies (0.68 THz, 0.918 THz, and 0.971 THz) within the metamaterial structure offers indispensable insights into the operational characteristics of the triple-band biosensor. The discernible high (red) and low (blue) intensity regions denote variations in surface power loss density, with the red regions indicating substantial surface power loss attributed to resonance effects. This amplified surface power loss is especially advantageous for terahertz imaging, enhancing the biosensor's utility in early cancer detection. The resonance-induced heightened surface power loss assumes a pivotal role in the interaction with cancer-specific biomolecules, thereby augmenting the biosensor's sensitivity and effectiveness in detecting subtle cellular changes associated with early-stage cancer. The intricacies of the observed patterns within the metamaterial structure are ascribed to the nuanced design, encompassing materials, structure, and dimensions. Discrepancies between Figs 13–15 emanate from distinctive resonance behaviors at each frequency, exerting influence on the location and distribution of high-intensity regions. Furthermore, elucidation of the color scale, ranging from 100,000 W/m^2 to 1,000,000 W/m^2, is imperative for the comprehensive contextualization and interpretation of intensity variations within the figures.
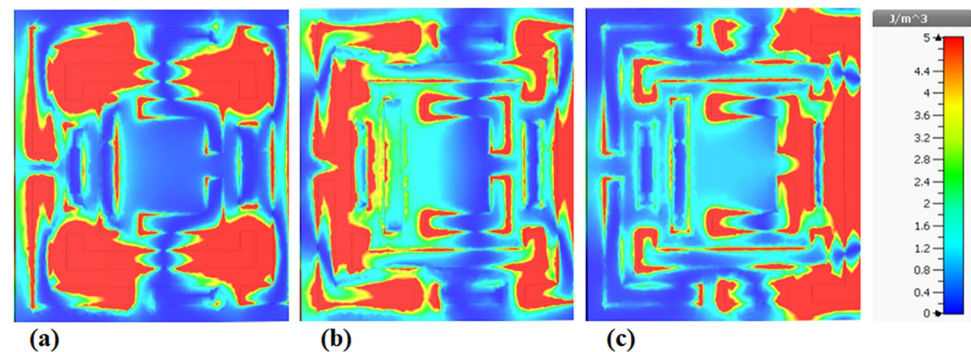
Fig 14. An examination of the electric energy density at: (a) at 0.684 THz, (b) at 0.918 THz, and (c) at 0.971 THz.

https://doi.org/10.1371/journal.pone.0311431.g014
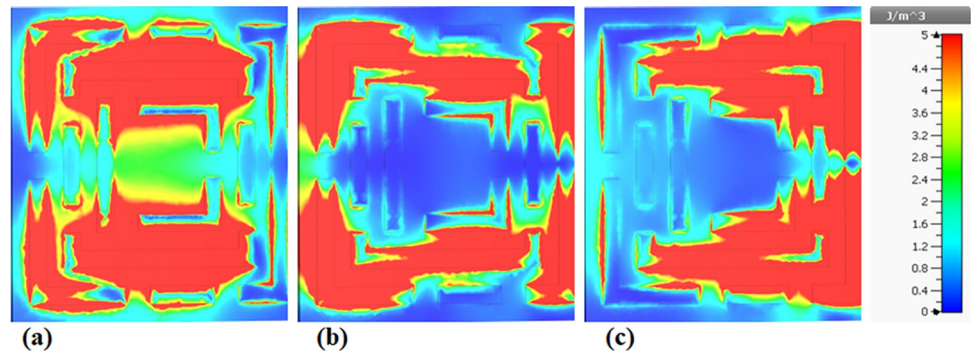
Fig 15. An examination of the magnetic energy density at: (a) at 0.684 THz, (b) at 0.918 THz, and (c) at 0.971 THz.

https://doi.org/10.1371/journal.pone.0311431.g015

4. Diagnosis of cervical cancer

The cervical cancer diagnostic biosensor integrates advanced technology to detect and diagnose cervical cancer in its early stages, overcoming present limitations. Utilizing microwave imaging (MWI), it enhances signal transmission and absorption analysis, improving the detection of cancer cells. Fig 16 illustrates the suggested detection of cervical cancer, employing two coverslips for error-free findings. A HeLa cell carcinoma sample, with a refractive index of 1.392 for malignant tissue and 1.368 for healthy cervical tissue, is positioned between the coverslips [57–61].

In Figs 17(A) and 18(A), the results of cervical cancer identification against healthy cervical tissue are presented. The examination focused on distinct peaks within the terahertz (THz) range. Fig 17(B) highlights a substantial difference between clean cervical tissue and cervical cancer, corresponding to 0.00119 THz (1190 MHz). Similarly, Fig 18(B) illustrates a significant distinction of 0.00163 THz (1630 MHz) between healthy cervical tissue and cervical cancer, observed in the third peak between 0.930 THz and 0.942 THz. These findings underscore the efficacy of terahertz imaging in discriminating between healthy and malignant cervical tissues, providing valuable insights for early cancer detection applications.

Fig 18 illustrates the absorption coefficients for normal and cancerous cervical tissues across the 0–1 THz frequency range, with a focused view from 0.930 to 0.942 THz. The biosensor's
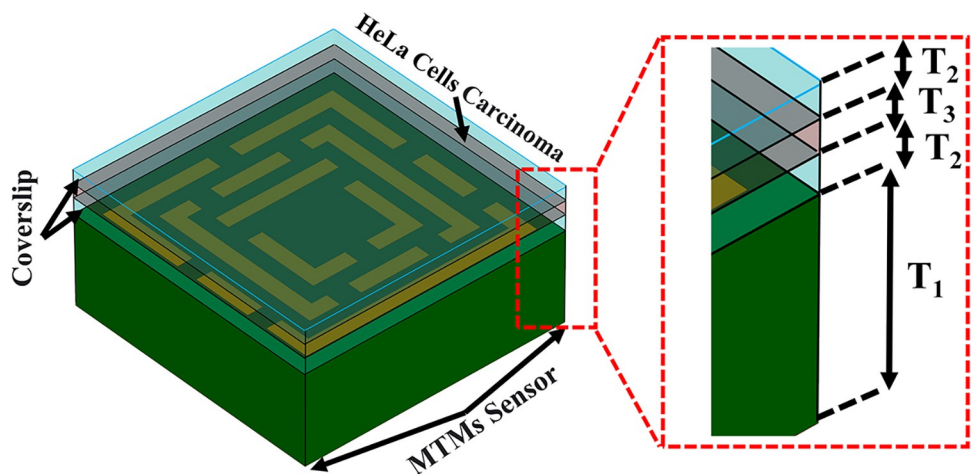
Fig 16. The suggested biosensor investigates the absorption coefficient in both healthy cervical and cervical-cancer.

https://doi.org/10.1371/journal.pone.0311431.g016

Fig 17. The proposed biosensor detects the absorption coefficients for normal Cervical and Cervical cancer; the frequency range is between: (a) 0–1 THz, (b) 0.663–0.670 THz.

functionality in the THz range is demonstrated by detecting and distinguishing between healthy and malignant tissues based on their distinct absorption characteristics. While absorption coefficients can sometimes be inconsistent due to tissue heterogeneity and measurement conditions, the frequency shift observed between healthy and cancerous tissues provides a more reliable diagnostic indicator. Specifically, the cancerous tissue shows a notable frequency shift at the third resonant peak compared to the normal tissue. This frequency shift, centered at approximately 0.93536 THz for cancerous tissue and 0.93699 THz for normal tissue, is a robust marker for identifying malignant tissue. The metamaterial-based design of the
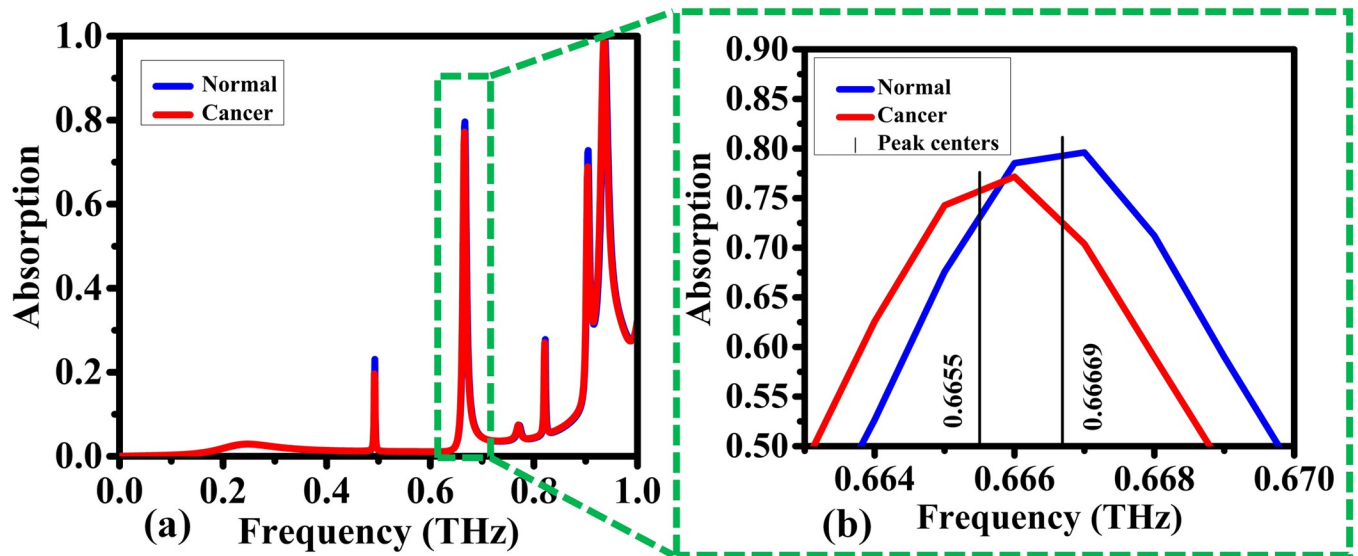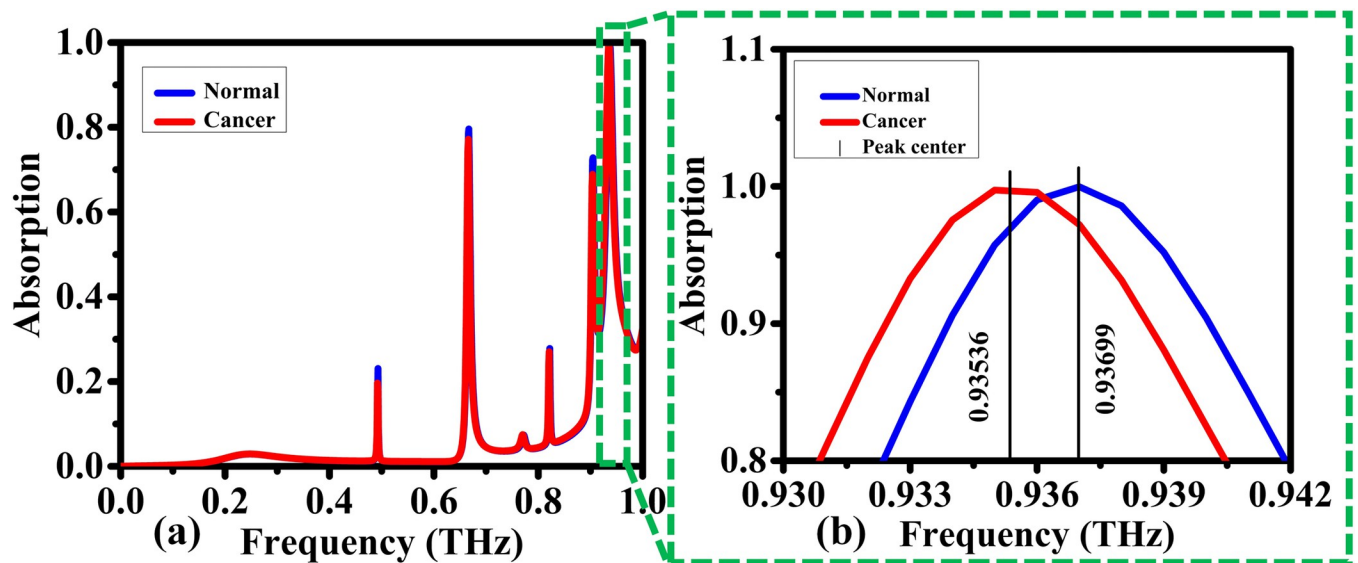

Fig 18. The proposed biosensor detects the absorption coefficients for normal Cervical and Cervical cancer; the frequency range is between: (a) 0–1 THz, (b) 0.930–0.942 THz.

biosensor enhances its sensitivity, allowing it to operate as a perfect absorber at specific resonant frequencies, thereby providing a dependable method for early-stage cervical cancer diagnosis.

In the assessment of triple-band perfect absorber metamaterials serving as sensors, critical parameters include the sensitivity (S), Figure of Merit (FOM) and the quality factor (Q factor). The FOM quantifies sensor efficacy by dividing a key performance parameter, such as sensitivity, by another relevant metric like bandwidth or noise level. Simultaneously, the dimensionless Q factor evaluates the resonance quality of the system. Elevated values of both FOM and Q coefficients in sensing applications signify heightened sensor performance. Sensitivity of perfect metamaterial absorbers, gauged by their response to variations in the surrounding medium's refractive index, is evaluated through the absorber's resonance frequency or absorption peak shift. The observed heightened sensitivity suggests its potential for discerning subtle refractive index changes, making it suitable for applications such as early cancer detection. Sensitivity plays a pivotal role in securing accurate results, especially when confronted with minimal refractive index fluctuations. A comprehensive evaluation of a sensor's efficiency and applicability in diverse sensing applications is derived from the full output measurement FOM, embodying its selectivity calculated as sensitivity normalized to the full width at half maximum (FWHM) of the resonant dip.

$$FOM = \frac{S}{FWHM} \tag{2}$$

The sharpness of the resonance is measured using the formula-based Q_{factor}.

$$Q_{factor} = \frac{\lambda}{FWHM} \tag{3}$$

Resonant wavelength, denoted by λ. Terahertz (THz) biosensors significantly increase the sensitivity of terahertz (THz) detection when used in a metamaterial-oriented manner. In scientific literature, sensitivity is commonly interpreted in two ways. The first is frequency sensitivity.

$$S = \frac{\Delta f}{\Delta n} \tag{4}$$

where Δf is the resonance peak's frequency shift and Δn are the change in refractive index (RI), which is frequently expressed in terms of refractive index units (RIU). An alternative approach is to compute S = ΔI/Δn, the intensity frequency, in which ΔI represents the resonance intensity variation [62, 63].

A penicillin detection biosensor, leveraging metamaterial technology, exhibits notable performance metrics, including a figure of merit (FOM) of 0.1216 RIU-1, a quality factor of 5.58, and sensitivity (S) of 0.02432 THz/RIU [64]. A distinct biosensor tailored for breast cancer detection displays a quality factor of 2.43, a figure of merit (FOM) of 2.75 RIU-1, and a sensitivity (S) of 1.21 THz/RIU [65]. Additionally, a biosensor designed for avian influenza virus detection showcases a sensitivity (S) of 1.06 THz/RIU and a figure of merit (FOM) of 0.166 RIU-1, although the quality factor is not explicitly provided [66]. Furthermore, our prior research conducted in 2023 introduced a dual-band biosensor tailored for the early detection of nonmelanoma skin cancer. The biosensor exhibited notable performance metrics, including a figure of merit (FOM) of 0.86 and 1.15 RIU-1, a quality factor of 12.8 and 13.5, and sensitivity (S) of 0.0515 and 0.076 THz/RIU, correspondingly for the first and second peaks. We have proposed a biosensor in this paper, compared with the results obtained in the above-mentioned papers, we believe will be a good alternative as a biosensor for detecting early detection

of cervical cancer. The proposed biosensor features three resonance bands, each characterized by specific quality factors, figures of merit, and sensitivities. The first resonance band exhibits a Q-factor of 85.77, FOM of 6.3 RIU^{-1}, and S of 0.049 THz/RIU. Since second resonance has not reached perfect absorber (80%) hence we neglect it. Also, the third resonance band demonstrates a Q-factor of 41.46, FOM of 3 RIU^{-1}, and S of 0.068 THz/RIU, particularly applied for cervical cancer diagnosis. The results indicate promising avenues for biosensing applications in cervical cancer research, showcasing the potential of terahertz imaging to enable accurate and early diagnosis, guiding timely interventions and treatments in healthcare settings, this biosensor represents a substantial development, as detailed in Table 2.

The study employed microwave imaging techniques in the terahertz band to validate the findings. A HeLa cell sample on a coverslip was tested using the proposed biosensor, as depicted in Fig 19. Terahertz E-field imaging with a triple-band, micron-sized metamaterial perfect absorber biosensor shows promise for detecting cervical cancer. The notable contrast in E-field intensity, as seen in Fig 20(A), suggests potential early-stage diagnostic capabilities, warranting further research for robust clinical translation. High E-field intensity hotspots corresponding to cervical cancer likely arise from distinct tissue dielectric properties and enhanced resonant interactions at specific terahertz frequencies, as shown in Fig 20(B). These hotspots indicate the potential presence of cervical cancer, with disparate dielectric properties affecting terahertz wave interactions. Molecules' vibrational resonances within tissue, like water and proteins, further contribute to differential dielectric properties, influencing terahertz wave propagation and scattering. This integrated understanding provides a comprehensive framework for interpreting hotspots, advancing non-invasive cervical cancer diagnostic methodologies. Furthermore, analogous investigations were undertaken for the subsequent selections of E-field. The E-field microwave imaging (MWI) technique results depicted in Fig 21 demonstrate the biosensor's effectiveness in detecting cervical cancer by analyzing electric field intensity variations at 0.918 THz. The images reveal distinct differences in electric field distribution between healthy and cancerous cervical tissues, with cancerous tissues exhibiting significant variations due to their higher permittivity and conductivity. These variations create

Table 2. Comparisons of bio-sensing performance of various sensor applications based on THz metamaterial.

Ref.	Year Published	FOM (RIU−1)	Q	S (THz/RIU)	Bio-application
[64]	2014	0.1216	5.58	0.02432	detection of Penicillia
[67]	2017	-	-	0.0242, 0.02438	detection of Virus
[68]	2019	258	14.93	0.658	Cancer detection
[69]	2020	-	-	0. 960	Biosensor, Collagen
[70]	2020	1.88	6.6	0.285	sensor
[71]	2021	-	10.64	1.65	Cancer detection
[41]	2021	-	-	0. 2833	Polystyrene particle
[72]	2021	-	-	0.074	Cervical cancer
[48]	2022	3.86	13	0.207	Cancer detection
[66]	2022	0.166	-	1.06	detection of avian influenza virus
[50]	2022	-	-	0.068	Hepatocellular carcinoma
[73]	2022	1.81, 1.57	8.21, 6.05	0. 203	sensor
[65]	2022	2.75	2.43	1.21	Cancer Diagnosi, Biosensor
[74]	2023	-	11	0.278	Bovin serum albumin protein
[75]	2023	-	82	0.495	Cancer detection
[22]	2023	0.86, 1.15	12.8, 13.5	0.0515, 0.076	Non-Melanoma Skin Cancer Diagnostics
This work	-	6.3, 3	85.77, 41.46	0.049, 0.068	Cervical cancer
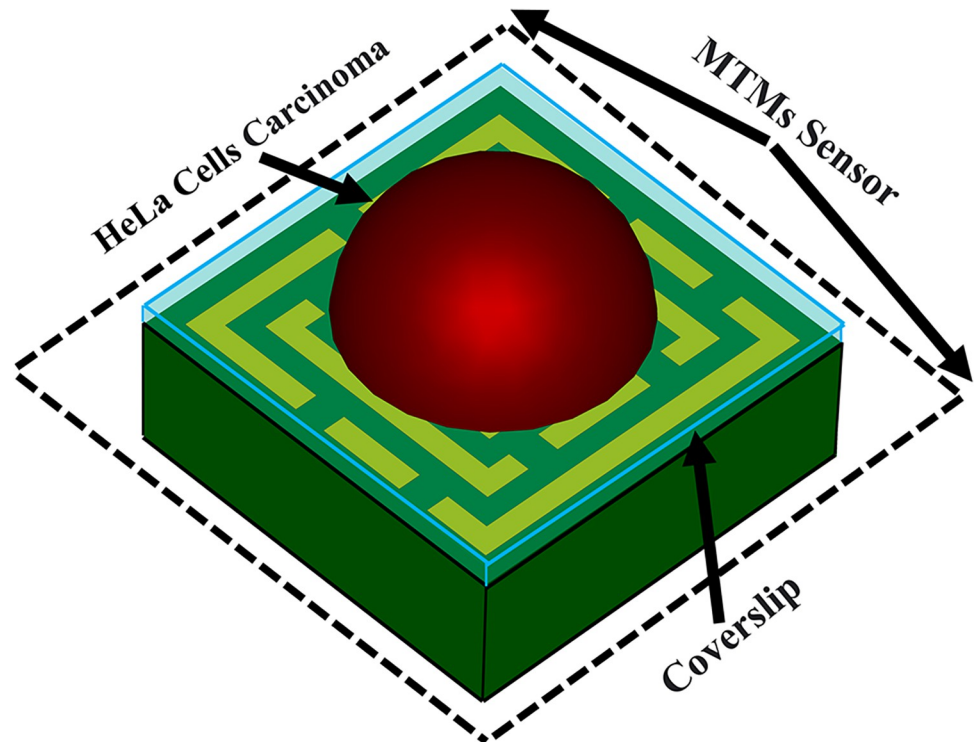
Fig 19. The diagnosis of cervical cancer using the MWI approach.

https://doi.org/10.1371/journal.pone.0311431.g019

detectable anomalies, which the biosensor, enhanced by its metamaterial-based design, can accurately identify. This sensitivity to electric field changes allows for non-invasive, early-stage cervical cancer detection, providing a rapid and patient-friendly alternative to traditional diagnostic methods. The findings highlight the biosensor's capability to not only detect cancer but also estimate the spatial extent of malignant regions, essential for effective diagnosis and treatment planning. Figs 21(A) and 22(A) delineate a zone characterized by diminished electric field intensity, indicative of a healthy cervical. Conversely, Figs 21(B) and 22(B) depict an area exhibiting heightened electric field intensity, suggestive of cervical cancer.
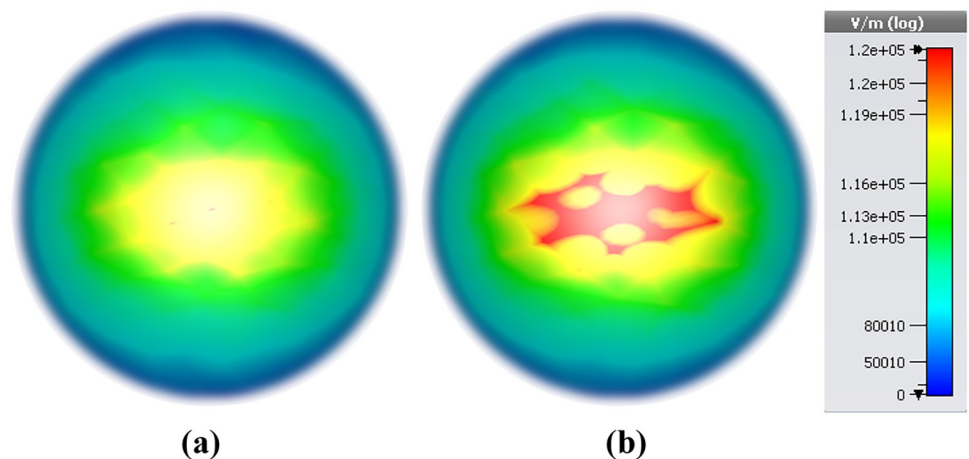
Fig 20. The E-field MWI technique results at 0.684 THz: (a) healthy Cervical, (b) Cervical cancer.

https://doi.org/10.1371/journal.pone.0311431.g020
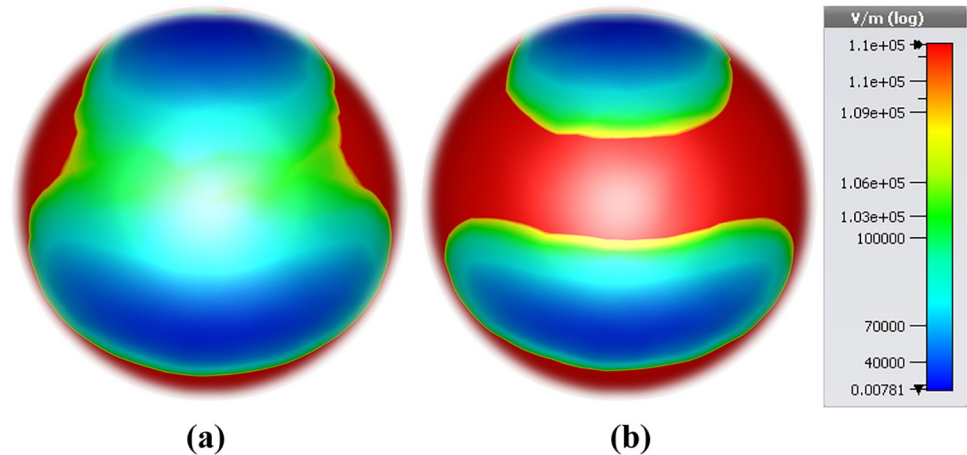
Fig 21. The E-field MWI technique results at 0.918 THz: (a) healthy Cervical, (b) Cervical cancer.

https://doi.org/10.1371/journal.pone.0311431.g021

The terahertz biosensor in our study employs advanced magnetic field (H- field) analysis to provide precise spatial insights into cervical tissue. By detecting nuanced deviations in magnetic field patterns that correlate with tissue dielectric properties, the biosensor effectively localizes and maps malignant lesions. This capability enhances diagnostic accuracy by distinguishing between healthy and cancerous tissues early in disease progression. These spatial insights not only facilitate timely intervention but also optimize treatment strategies tailored to individual patient needs, thereby advancing the efficacy of cervical cancer diagnostics and therapeutic outcomes. Exploration into magnetic fields for terahertz imaging shows promise in cervical cancer detection, notably with terahertz H-field imaging via microwave biosensors. An intense magnetic field envelops the specimen, yet within this field, a region of diminished magnetic field density is discernible, denoting a healthy cervical, as elucidated in Fig 23(A). Conversely, Fig 23(B) illustrates an area characterized by elevated magnetic field intensity at the center of the image, indicative of cervical carcinoma. This contrast aids early diagnosis, influenced by differing magnetic properties stemming from tissue composition and molecular distributions. Biosensor resonance at specific frequencies enhances local magnetic fields, potentially amplifying signals within cancerous tissue. Such findings underscore magnetic
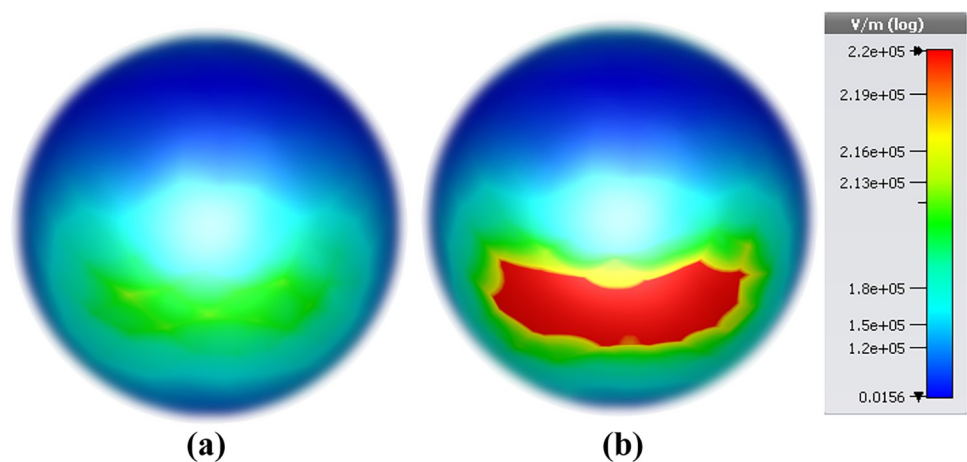
Fig 22. The E-field MWI technique results at 0.971 THz: (a) healthy Cervical, (b) Cervical cancer.

https://doi.org/10.1371/journal.pone.0311431.g022
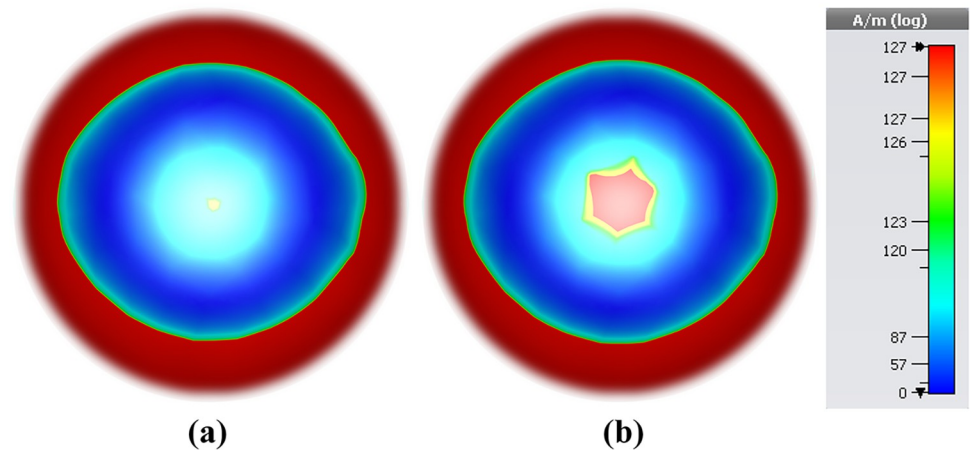
Fig 23. The H-field MWI technique results at 0.684 THz: (a) healthy Cervical, (b) Cervical cancer.

fields' potential in terahertz imaging for cervical cancer detection, warranting further research and clinical validation.

To further validate the biosensor's applicability for early cancer detection, supplementary investigations were conducted concerning electrical and magnetic energy density. Fig 24(A) depicts an area with low electrical energy density, suggesting healthy cells. In contrast, Fig 24 (B) reveals a region with markedly high electrical energy density, indicative of cancerous cells. Similarly, Fig 25 presents the magnetic energy density distribution at 0.684 THz for both healthy and cancerous cervical tissues, revealing insights into the biosensor's interaction with differing tissue types based on their distinct dielectric properties. In healthy tissue (Fig 25(A)), magnetic energy density shows a uniform distribution, predominantly centralized, indicating minimal magnetic field disturbance and consistent dielectric properties conducive to stable absorption patterns. Conversely, cancerous tissue (Fig 25(B)) displays heterogeneous magnetic energy density with irregular, intense regions, reflecting altered dielectric properties and significant disruption of the magnetic field due to the presence of cancerous cells. This disparity underscores the biosensor's efficacy in distinguishing between healthy and cancerous tissues,
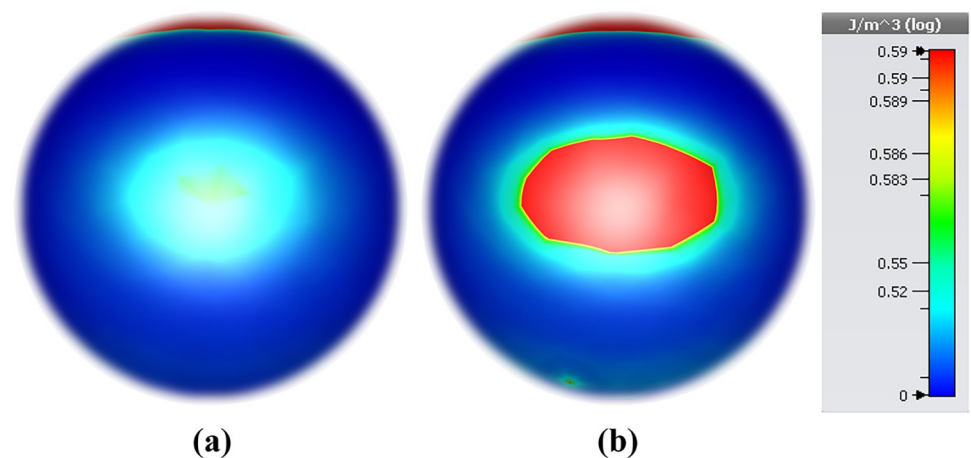
Fig 24. The electric energy density MWI technique results at 0.971 THz: (a) healthy Cervical, (b) Cervical cancer.

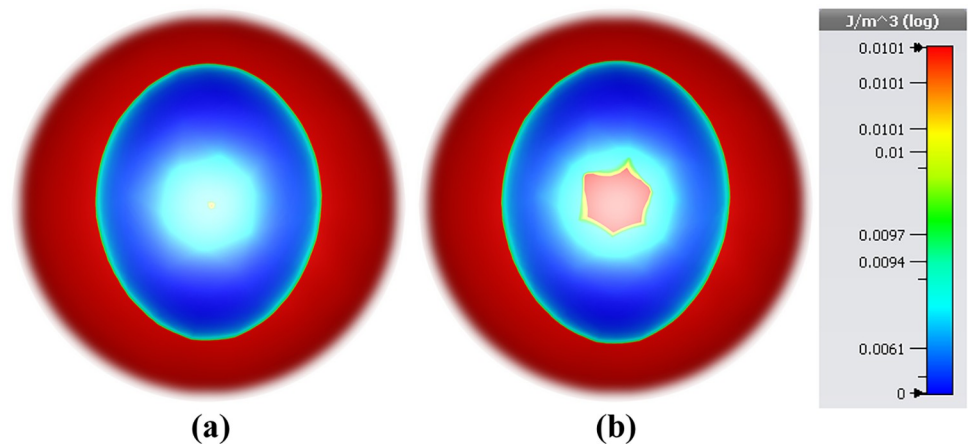**Fig 25.** The magnetic energy density MWI technique results at 0.684 THz: (a) healthy Cervical, (b) Cervical cancer.

https://doi.org/10.1371/journal.pone.0311431.g025

utilizing the irregular magnetic energy density patterns and heightened absorption in cancerous regions as robust indicators of malignancy. Leveraging magnetic energy density distributions enhances the biosensor's diagnostic precision, offering a reliable method for early-stage cervical cancer detection in the terahertz spectrum, even amidst varying absorption coefficients and tissue heterogeneity.

Our proposed terahertz biosensor, outlined in Table 3, differs from conventional microwave methods by utilizing frequency-domain data to detect changes in refractive index, providing spatial insights into the target. This suggests that biosensors could revolutionize Cervical cancer diagnostics by enabling more accurate detection of cancer indicators, facilitating early identification and treatment. Early-stage intervention is critical for improving prognosis and survival rates, making biosensors valuable tools for healthcare practitioners in detecting biomarkers associated with Cervical cancer.

Table 3. A comparison between the terahertz band study on perfect metamaterials and the recommended biosensor.

References	Material substrate	Frequency operating THz	Techniques used	Absorptivity	Application
[47]	Glass	0–0.37	Glass/InSb/MgF2/InSb	0.998	Colon Cancer Detection
[76]	SiO2	7–9.5	Au/SiO2/ Graphene	0.98	Multi-Frequency Broadband and Ultra-Broadband
[77]	silicon dioxide	1.5–1.7	Gold/silicon dioxide/ Gold	0.972, 0.991	biosensor for detecting coronaviruses
[65]	SiO2	0.5–2.5	SiO2/Graphene	-	Breast cancer detection
[78]	PET	0–3	PET/FSS/UV glue/ Graphene	0.99, 0.80, 0.95	Multifunctional Tunable Terahertz
[79]	SiO2	2–6	graphene/Au/SiO2/Au	0.99	Refractive index sensor
[43]	dielectric layer	1–3	Au/dielectric layer/Au	0.99, 0.99	Sensor
[80]	Topas spacer	0.5–4.5	graphene/Topas/Au	0.99, 0.98, 0.99	Ultra-Broadband Absorber
[81]	photonic crystal plate	1–3	bulk Dirac semimetal/photonic crystal/Au	0.97, 0.98, 0.99	Narrowband perfect absorber
[42]	dielectric Teflon	1–2.2	Au/dielectric Teflon/Au	0.99	Sensor
[82]	Teflon	0.7–5	Ion gel/Graphene/Teflon/Gold	>0.96	polarization-sensitive
This work	Polyimide	0–1	Al/ Polyimide /Al	0.9996, 0.992, 0.99877	Cervical cancer, Microwave Imaging and Biosensor

https://doi.org/10.1371/journal.pone.0311431.t003

5. Future perspective

Developing more sensitive biosensors for early cancer detection, such as terahertz (THz) electromagnetic (EM) wave imaging biosensors for the early identification of blood, colon, breast, adrenal gland (PC-12), and Non-Melanoma Skin Cancer (NMSC), among other cancers.

6. Conclusions

In this manuscript, we introduced an innovative structure of a biosensor intended for dependable early-stage diagnosis of cervical cancer. The proposed device operates within the terahertz (THz) spectrum. Its geometrical details are carefully developed to ensure triple-band operation as a perfect absorber, thereby enhancing sensitivity. An essential component of the sensor is a metamaterial layer, which facilitates realization of the required absorption characteristics. The operating principles of the device involve discriminating between healthy and cancerous tissue based on their different dielectric properties. Suitability of the suggested sensor for cervical cancer detection has been demonstrated through comprehensive numerical studies. In particular, a number of specific case studies were carried out involving healthy and cancer-affected cervical. The analysis of magnetic field strength allows for detecting the latter as well as for determination of its spatial extent. The proposed sensor was also compared to a number of state-of-the-art designs reported in the literature showing its competitive performance, also in terms of utilizing unconventional approach (here, the employment of frequency-domain data for detecting changes in refractive index).

Author Contributions

Conceptualization: Musa N. Hamza, Mohammad Tariqul Islam, Sunil Lavadiya, Iftikhar ud Din, Bruno Sanches, Slawomir Koziel, Md. Shabiul Islam.

Data curation: Musa N. Hamza.

Formal analysis: Musa N. Hamza.

Funding acquisition: Mohammad Tariqul Islam, Slawomir Koziel, Md. Shabiul Islam.

Investigation: Musa N. Hamza, Mohammad Tariqul Islam, Sunil Lavadiya, Iftikhar ud Din, Bruno Sanches, Slawomir Koziel, Md. Shabiul Islam.

Methodology: Musa N. Hamza, Mohammad Tariqul Islam, Sunil Lavadiya, Iftikhar ud Din, Bruno Sanches, Slawomir Koziel.

Project administration: Mohammad Tariqul Islam.

Resources: Musa N. Hamza, Mohammad Tariqul Islam, Sunil Lavadiya, Iftikhar ud Din, Bruno Sanches, Slawomir Koziel, Md. Shabiul Islam.

Software: Musa N. Hamza, Sunil Lavadiya.

Supervision: Mohammad Tariqul Islam.

Validation: Musa N. Hamza, Sunil Lavadiya, Bruno Sanches, Slawomir Koziel, Md. Shabiul Islam.

Visualization: Musa N. Hamza, Mohammad Tariqul Islam, Sunil Lavadiya, Iftikhar ud Din, Bruno Sanches, Slawomir Koziel, Md. Shabiul Islam.

Writing – original draft: Musa N. Hamza, Sunil Lavadiya, Iftikhar ud Din, Bruno Sanches, Slawomir Koziel.

Writing – review & editing: Mohammad Tariqul Islam, Sunil Lavadiya, Iftikhar ud Din, Bruno Sanches, Slawomir Koziel, Md. Shabiul Islam.

References

1. Kim WC, Kim GE, Suh CO, Loh JJ: High versus low dose rate intracavitary irradiation for adenocarcinoma of the uterine cervix. *Japanese journal of clinical oncology* 2001, 31:432–437. https://doi.org/10.1093/jjco/hye098 PMID: 11689597

2. Vos T, Allen C, Arora M, Barber RM, Bhutta ZA, Brown A, et al: Global, regional, and national incidence, prevalence, and years lived with disability for 310 diseases and injuries, 1990–2015: a systematic analysis for the Global Burden of Disease Study 2015. *The lancet* 2016, 388:1545–1602. https://doi.org/10.1016/S0140-6736(16)31678-6 PMID: 27733282

3. Zeng H, Chen W, Zheng R, Zhang S, Ji JS, Zou X, et al: Changing cancer survival in China during 2003–15: a pooled analysis of 17 population-based cancer registries. *The Lancet Global Health* 2018, 6:e555–e567. https://doi.org/10.1016/S2214-109X(18)30127-X PMID: 29653628

4. Egemen D, Perkins RB, Cheung LC, Befano B, Rodriguez AC, Desai K, et al: Artificial intelligence–based image analysis in clinical testing: lessons from cervical cancer screening. *JNCI: Journal of the National Cancer Institute* 2024, 116:26–33. https://doi.org/10.1093/jnci/djad202 PMID: 37758250

5. de Sanjosé S, Perkins RB, Campos N, Inturrisi F, Egemen D, Befano B, et al: Design of the HPV-Automated Visual Evaluation (PAVE) study: validating a novel cervical screening strategy. *Elife* 2024, 12: RP91469. https://doi.org/10.7554/eLife.91469 PMID: 38224340

6. Inturrisi F, de Sanjosé S, Desai KT, Dagnall C, Egemen D, Befano B, et al: A rapid HPV typing assay to support global cervical cancer screening and risk-based management: A cross-sectional study. *International journal of cancer* 2024, 154:241–250. https://doi.org/10.1002/ijc.34698 PMID: 37772799

7. Sun Y: Facing challenges: Development of cytology technique in the last century. *Zhonghua Bing li xue za zhi = Chinese Journal of Pathology* 2003, 32:283–285. PMID: 14518445

8. Solomon D, Stoler M, Jeronimo J, Khan M, Castle P, Schiffman M: Diagnostic utility of endocervical curettage in women undergoing colposcopy for equivocal or low-grade cytologic abnormalities. *Obstetrics & gynecology* 2007, 110:288–295. https://doi.org/10.1097/01.AOG.0000270154.69879.09 PMID: 17666602

9. Katki HA, Kinney WK, Fetterman B, Lorey T, Poitras NE, Cheung L, et al: Cervical cancer risk for women undergoing concurrent testing for human papillomavirus and cervical cytology: a population-based study in routine clinical practice. *The lancet oncology* 2011, 12:663–672. https://doi.org/10.1016/S1470-2045(11)70145-0 PMID: 21684207

10. Arbyn M, Walker A, Meijer CJ: HPV-based cervical-cancer screening in China. *The Lancet Oncology* 2010, 11:1112–1113. https://doi.org/10.1016/S1470-2045(10)70262-X PMID: 21075053

11. Hou D, Li X, Cai J, Ma Y, Kang X, Huang P, et al: Terahertz spectroscopic investigation of human gastric normal and tumor tissues. *Physics in Medicine & Biology* 2014, 59:5423. https://doi.org/10.1088/0031-9155/59/18/5423 PMID: 25164759

12. Wahaia F, Valusis G, Bernardo LM, Almeida A, Moreira JA, Lopes PC, et al: Detection of colon cancer by terahertz techniques. *Journal of Molecular Structure* 2011, 1006:77–82.

13. Taylor ZD, Garritano J, Sung S, Bajwa N, Bennett DB, Nowroozi B, et al: THz and mm-wave sensing of corneal tissue water content: electromagnetic modeling and analysis. *IEEE transactions on terahertz science and technology* 2015, 5:170–183. https://doi.org/10.1109/TTHZ.2015.2392619 PMID: 26322247

14. Yoneyama H, Yamashita M, Kasai S, Kawase K, Ueno R, Ito H, et al: Terahertz spectroscopy of native-conformation and thermally denatured bovine serum albumin (BSA). *Physics in Medicine & Biology* 2008, 53:3543. https://doi.org/10.1088/0031-9155/53/13/010 PMID: 18552417

15. Zhu Z, Cheng C, Chang C, Ren G, Zhang J, Peng Y, et al: Characteristic fingerprint spectrum of neurotransmitter norepinephrine with broadband terahertz time-domain spectroscopy. *Analyst* 2019, 144:2504–2510. https://doi.org/10.1039/c8an02079e PMID: 30638228

16. Mittleman DM: Twenty years of terahertz imaging. *Optics express* 2018, 26:9417–9431.

17. Eadie LH, Reid CB, Fitzgerald AJ, Wallace VP: Optimizing multi-dimensional terahertz imaging analysis for colon cancer diagnosis. *Expert Systems with Applications* 2013, 40:2043–2050.

18. Chen H, Ma S-H, Yan W-X, Wu X-M, Wang X-Z: The diagnosis of human liver cancer by using THz fiber-scanning near-field imaging. *Chinese Physics Letters* 2013, 30:030702.

19. Hamza MN, Islam MT: Design of MTM-based Multi-band Micro-Biosensor in Terahertz region as perfect absorber for Early-Stage Leukemia Diagnosis with sensitivity 18626373 THz/RIU. *IEEE Sensors Journal* 2024.

20. Fitzgerald AJ, Wallace VP, Jimenez-Linan M, Bobrow L, Pye RJ, Purushotham AD, et al: Terahertz pulsed imaging of human breast tumors. *Radiology* 2006, 239:533–540. https://doi.org/10.1148/radiol. 2392041315 PMID: 16543586

21. Joseph CS, Yaroslavsky AN, Neel VA, Goyette TM, Giles RH: Continuous wave terahertz transmission imaging of nonmelanoma skin cancers. *Lasers in Surgery and Medicine* 2011, 43:457–462. https://doi. org/10.1002/lsm.21078 PMID: 21761415

22. Hamza MN, Islam MT: Designing an Extremely Tiny Dual-Band Biosensor Based on MTMs in the Terahertz Region as a Perfect Absorber for Non-Melanoma Skin Cancer Diagnostics. *IEEE Access* 2023, 11:136770–136781.

23. Hamza MN, Islam MT, Lavadiya S, Koziel S, Ud Din I, Sanches B: Designing a High-sensitivity Dual-band Nano-Biosensor based on Petahertz MTMs to provide a perfect absorber for Early-Stage Non-Melanoma Skin Cancer diagnostic. *IEEE Sensors Journal* 2024.

24. Hamza MN, Islam MT, Koziel S, Hamad MA, ud Din I, Farmani A, et al: Designing a High-sensitivity Microscale Triple-band Biosensor based on Terahertz MTMs to provide a perfect absorber for Non-Melanoma Skin Cancer diagnostic. *IEEE Photonics Journal* 2024.

25. Ashworth PC, Pickwell-MacPherson E, Provenzano E, Pinder SE, Purushotham AD, Pepper M, et al: Terahertz pulsed spectroscopy of freshly excised human breast cancer. *Optics express* 2009, 17:12444–12454. https://doi.org/10.1364/oe.17.012444 PMID: 19654646

26. Chen H, Lee W-J, Huang H-Y, Chiu C-M, Tsai Y-F, Tseng T-F, et al: Performance of THz fiber-scanning near-field microscopy to diagnose breast tumors. *Optics Express* 2011, 19:19523–19531. https://doi. org/10.1364/OE.19.019523 PMID: 21996893

27. Kolesnikov AS, Kolesnikova EA, Tuchina DK, Terentyuk AG, Nazarov M, Skaptsov AA, et al: In-vitro terahertz spectroscopy of rat skin under the action of dehydrating agents. In *Saratov Fall Meeting 2013*: *Optical Technologies in Biophysics and Medicine XV; and Laser Physics and Photonics XV*. SPIE; 2014: 92–98.

28. Mahmud MZ, Islam MT, Misran N, Kibria S, Samsuzzaman M: Microwave imaging for breast tumor detection using uniplanar AMC based CPW-fed microstrip antenna. *IEEE Access* 2018, 6:44763–44775.

29. Rahman A, Islam MT, Singh MJ, Kibria S, Akhtaruzzaman M: Electromagnetic performances analysis of an ultra-wideband and flexible material antenna in microwave breast imaging: To implement a wearable medical bra. *Scientific reports* 2016, 6:38906. https://doi.org/10.1038/srep38906 PMID: 28008923

30. Rokunuzzaman M, Samsuzzaman M, Islam MT: Unidirectional wideband 3-D antenna for human head-imaging application. *IEEE Antennas and Wireless Propagation Letters* 2016, 16:169–172.

31. Rashed ANZ, Mohammed AE-NA, Zaky WF, Amiri I, Yupapin P: The switching of optoelectronics to full optical computing operations based on nonlinear metamaterials. *Results in Physics* 2019, 13:102152.

32. Veselago VG: The electrodynamics of substances with simultaneously negative values of img align = absmiddle Alt = ϵ Eps/Img and μ. *Physics-Uspekhi* 1968, 10:509–514.

33. Misran N, Yusop SH, Islam MT, Ismail MY: Analysis of parameterization substrate thickness and permittivity for concentric split ring square reflectarray element. *Jurnal Kejuruteraan (Journal of Engineering)* 2012, 23:11–16.

34. Chowdhury IH, Mazumder MMR, Islam SS, Islam MT, Soliman MS, Islam MS: Ultrawideband nanostructured metamaterial absorber with an Octagon-Packed Star-Shaped resonator for UV to NIR spectrum wavelength application. *Ain Shams Engineering Journal* 2024:102653.

35. Hanif A, Alam T, Islam MT, Hakim ML, Yahya I, Albadran S, et al: Ni-PI-Ni based nanoarchitectonics near-perfect metamaterial absorber with incident angle stability for visible and near-infrared applications. *International Journal of Optomechatronics* 2024, 18:2299026.

36. Mahmud S, Karim M, Islam SS, Shuvo MMK, Akter T, Almutairi AF, et al: A multi-band near perfect polarization and angular insensitive metamaterial absorber with a simple octagonal resonator for visible wavelength. *IEEE Access* 2021, 9:117746–117760.

37. Yan Z, Tang C, Wu G, Tang Y, Gu P, Chen J, et al: Perfect absorption and refractive-index sensing by metasurfaces composed of cross-shaped hole arrays in metal substrate. *Nanomaterials* 2020, 11:63. https://doi.org/10.3390/nano11010063 PMID: 33383802

38. Stanley R: Plasmonics in the mid-infrared. *Nature Photonics* 2012, 6:409–411.

39. Chen HT, O'Hara JF, Azad AK, Taylor AJ: Manipulation of terahertz radiation using metamaterials. *Laser & Photonics Reviews* 2011, 5:513–533.

40. Huang L, Chen H-T: A brief review on terahertz metamaterial perfect absorbers. *Terahertz Sci Technol* 2013, 6:26–39.

41. Yang J, Lin Y-S: Design of tunable terahertz metamaterial sensor with single-and dual-resonance characteristic. *Nanomaterials* 2021, 11:2212. https://doi.org/10.3390/nano11092212 PMID: 34578528

42. Saadeldin AS, Hameed MFO, Elkaramany EM, Obayya SS: Highly sensitive terahertz metamaterial sensor. *IEEE Sensors Journal* 2019, 19:7993–7999.

43. Wang B-X, He Y, Lou P, Xing W: Design of a dual-band terahertz metamaterial absorber using two identical square patches for sensing application. *Nanoscale Advances* 2020, 2:763–769. https://doi.org/10.1039/c9na00770a PMID: 36133238

44. Azab MY, Hameed MFO, Obayya SS: Overview of Optical Biosensors for Early Cancer Detection: Fundamentals, Applications and Future Perspectives. *Biology* 2023, 12:232. https://doi.org/10.3390/biology12020232 PMID: 36829508

45. Geng Z, Zhang X, Fan Z, Lv X, Chen H: A route to terahertz metamaterial biosensor integrated with microfluidics for liver cancer biomarker testing in early stage. *Scientific reports* 2017, 7:16378. https://doi.org/10.1038/s41598-017-16762-y PMID: 29180650

46. Banerjee S, Nath U, Dutta P, Jha AV, Appasani B, Bizon N: A theoretical terahertz metamaterial absorber structure with a high quality factor using two circular ring resonators for biomedical sensing. *Inventions* 2021, 6:78.

47. Vafapour Z, Troy W, Rashidi A: Colon cancer detection by designing and analytical evaluation of a water-based THz metamaterial perfect absorber. *IEEE Sensors Journal* 2021, 21:19307–19313.

48. Patel SK, Surve J, Parmar J: Detection of cancer with graphene metasurface-based highly efficient sensors. *Diamond and Related Materials* 2022, 129:109367.

49. Askari M, Farrokhi Z, Pakarzadeh H: Design proposal for highly sensitive infrared metamaterial-based sensors. *Optical and Quantum Electronics* 2022, 54:737.

50. Bhati R, Malik AK: Ultra-efficient terahertz metamaterial sensor. *Results in Optics* 2022, 8:100236.

51. Ma S, Zhang P, Mi X, Zhao H: Highly sensitive terahertz sensor based on graphene metamaterial absorber. *Optics Communications* 2023, 528:129021.

52. Jain P, Prakash K, Sardana N, Kumar S, Gupta N, Singh AK: Design of an ultra-thin hepta-band metamaterial absorber for sensing applications. *Optical and Quantum Electronics* 2022, 54:569.

53. Jain P, Singh AK, Pandey JK, Bansal S, Sardana N, Kumar S, et al: An ultrathin compact polarization-sensitive triple-band microwave metamaterial absorber. *Journal of Electronic Materials* 2021, 50:1506–1513.

54. Jain P, Bansal S, Prakash K, Sardana N, Gupta N, Kumar S, et al: Graphene-based tunable multi-band metamaterial polarization-insensitive absorber for terahertz applications. *Journal of Materials Science*: *Materials in Electronics* 2020, 31:11878–11886.

55. Jain P, Singh AK, Pandey JK, Garg S, Bansal S, Agarwal M, et al: Ultra-thin metamaterial perfect absorbers for single-/dual-/multi-band microwave applications. *IET Microwaves*, *Antennas & Propagation* 2020, 14:390–396.

56. Jain P, Prakash K, Khanal GM, Sardana N, Kumar S, Gupta N, et al: Quad-band polarization sensitive terahertz metamaterial absorber using Gemini-shaped structure. *Results in Optics* 2022, 8:100254.

57. Ahmed K, Paul BK, Ahmed F, Jabin MA, Uddin MS: Numerical demonstration of triangular shaped photonic crystal fibre-based biosensor in the Terahertz range. *IET Optoelectronics* 2021, 15:1–7.

58. Jabin MA, Ahmed K, Rana MJ, Paul BK, Islam M, Vigneswaran D, et al: Surface plasmon resonance based titanium coated biosensor for cancer cell detection. *IEEE Photonics Journal* 2019, 11:1–10.

59. Kumar P, Kumar V, Roy JS: Dodecagonal photonic crystal fibers with negative dispersion and low confinement loss. *Optik* 2017, 144:363–369.

60. Parvin T, Ahmed K, Alatwi AM, Rashed ANZ: Differential optical absorption spectroscopy-based refractive index sensor for cancer cell detection. *Optical Review* 2021, 28:134–143.

61. Sharma P, Sharan P, Deshmukh P: A photonic crystal sensor for analysis and detection of cancer cells. In *2015 International conference on pervasive computing (ICPC)*. IEEE; 2015: 1–5.

62. Gómez-Castaño M, Garcia-Pomar JL, Pérez LA, Shanmugathasan S, Ravaine S, Mihi A: Electrodeposited negative index metamaterials with visible and near infrared response. *Advanced Optical Materials* 2020, 8:2000865.

63. Krause R, Chávez-Cervantes M, Aeschlimann S, Forti S, Fabbri F, Rossi A, et al: Ultrafast charge separation in bilayer WS2/graphene heterostructure revealed by time-and angle-resolved photoemission spectroscopy. *Frontiers in Physics* 2021, 9:668149.

64. Park S, Hong J, Choi S, Kim H, Park W, Han S, et al: Detection of microorganisms using terahertz metamaterials. *Scientific reports* 2014, 4:4988. https://doi.org/10.1038/srep04988 PMID: 24832607

65. Tan C, Wang S, Li S, Liu X, Wei J, Zhang G, et al: Cancer Diagnosis Using Terahertz-Graphene-Metasurface-Based Biosensor with Dual-Resonance Response. *Nanomaterials* 2022, 12:3889. https://doi.org/10.3390/nano12213889 PMID: 36364665

66. Hoseini E, Mir A, Farmani A: Modeling and proposal of a black phosphorus-based nanostructure for detection of avian influenza virus in infrared region. *Optical and Quantum Electronics* 2022, 54:609.

67. Park S, Cha S, Shin G, Ahn Y: Sensing viruses using terahertz nano-gap metamaterials. *Biomedical optics express* 2017, 8:3551–3558. https://doi.org/10.1364/BOE.8.003551 PMID: 28856034

68. Nejad HE, Mir A, Farmani A: Supersensitive and tunable nano-biosensor for cancer detection. *IEEE Sensors Journal* 2019, 19:4874–4881.

69. Asgari S, Granpayeh N, Fabritius T: Controllable terahertz cross-shaped three-dimensional graphene intrinsically chiral metastructure and its biosensing application. *Optics Communications* 2020, 474:126080.

70. Chen T, Zhang D, Huang F, Li Z, Hu F: Design of a terahertz metamaterial sensor based on split ring resonator nested square ring resonator. *Materials Research Express* 2020, 7:095802.

71. Azab MY, Hameed MFO, Nasr AM, Obayya S: Highly sensitive metamaterial biosensor for cancer early detection. *IEEE Sensors Journal* 2021, 21:7748–7755.

72. Li D, Hu F, Zhang H, Chen Z, Huang G, Tang F, et al: Identification of early-stage cervical cancer tissue using metamaterial terahertz biosensor with two resonant absorption frequencies. *IEEE Journal of Selected Topics in Quantum Electronics* 2021, 27:1–7.

73. Hu H, Qi B, Zhao Y, Zhang X, Wang Y, Huang X: A graphene-based THz metasurface sensor with air-spaced structure. *Frontiers in Physics* 2022, 10:990126.

74. Shen Y, Li X, Wang J, Liu H, Jing J, Deng X, et al: Low-Concentration Biological Sample Detection Using an Asymmetric Split Resonator Terahertz Metamaterial. In *Photonics*. MDPI; 2023: 111.

75. Mezache Z, Hafdi Z, Tao J: Design of a novel graphene buzzle metamaterial refractometer for sensing of cancerous cells in the terahertz regime. *Optik* 2023, 287:171170.

76. Chen Z, Cai P, Wen Q, Chen H, Tang Y, Yi Z, et al: Graphene Multi-Frequency Broadband and Ultra-Broadband Terahertz Absorber Based on Surface Plasmon Resonance. *Electronics* 2023, 12:2655.

77. El-Wasif Z, Ismail T, Hamdy O: Design and optimization of highly sensitive multi-band terahertz meta-material biosensor for coronaviruses detection. *Optical and Quantum Electronics* 2023, 55:604. https://doi.org/10.1007/s11082-023-04906-6 PMID: 37215398

78. Zhuang S, Li X, Yang T, Sun L, Kosareva O, Gong C, et al: Graphene-Based Absorption–Transmission Multi-Functional Tunable THz Metamaterials. *Micromachines* 2022, 13:1239. https://doi.org/10.3390/mi13081239 PMID: 36014160

79. Nickpay M-R, Danaie M, Shahzadi A: Highly sensitive THz refractive index sensor based on folded split-ring metamaterial graphene resonators. *Plasmonics* 2021:1–12.

80. Liu L, Liu W, Song Z: Ultra-broadband terahertz absorber based on a multilayer graphene metamaterial. *Journal of Applied Physics* 2020, 128.

81. Wang Y, Yi Y, Xu D, Yi Z, Li Z, Chen X, et al: Terahertz tunable three band narrowband perfect absorber based on Dirac semimetal. *Physica E*: *Low-dimensional Systems and Nanostructures* 2021, 131:114750.

82. Asgari S, Fabritius T: Numerical Simulation and Equivalent Circuit Model of Multi-Band Terahertz Absorber Composed of Double-Sided Graphene Comb Resonator Array. *IEEE Access* 2023.